Investigation of the metabolomic crosstalk between liver sinusoidal endothelial cells and hepatocytes exposed to paracetamol using organ-on-chip technology

Taha Messelmani, Anne Le Goff, Fabrice Soncin, Françoise Gilard, Zied Souguir, Nathalie Maubon, Bertrand Gakière, Cécile Legallais, Eric Leclerc, Rachid Jellali

Investigation of the metabolomic crosstalk between liver sinusoidal endothelial cells and hepatocytes exposed to paracetamol using organ-on-chip technology

Taha Messelmani [1], Anne Le Goff [1], Fabrice Soncin [2,3], Françoise Gilard [4], Zied Souguir [5], Nathalie Maubon [5], Bertrand Gakière [4], Cécile Legallais [1], Eric Leclerc [1,3], Rachid Jellali [1]*

[1]*Université de technologie de Compiègne, CNRS, Biomechanics and Bioengineering, Centre de recherche Royallieu CS 60319, 60203 Compiègne Cedex, France*
[2] *CNRS/IIS/Centre Oscar Lambret/Lille University SMMiL-E Project, CNRS Délégation Hauts-de-France, 43 Avenue le Corbusier, 59800 Lille, France*
[3]*CNRS IRL 2820, Laboratory for Integrated Micro Mechatronic Systems, Institute of Industrial Science, University of Tokyo, 4-6-1 Komaba, Meguro-ku, Tokyo, Japan*
[4]*Institute of Plant Sciences Paris-Saclay (IPS2), UMR 9213/UMR1403, CNRS, INRA, Université Paris-Sud, Université d'Evry, Université Paris-Diderot, Université Paris Saclay, Bâtiment 630 Rue Noetzlin, 91192, Gif-sur-Yvette Cedex, France*
[5]*HCS Pharma, 250 rue Salvador Allende, Biocentre Fleming Bâtiment A, 59120 Loos, France*

*** Corresponding author: rachid.jellali@utc.fr**

Abstract

Organ-on-chip technology is a promising *in vitro* approach recapitulating human physiology for the study of responses to drug exposure. Organ-on-chip cell cultures have paved new grounds for testing and understanding metabolic dose-responses when evaluating pharmaceutical and environmental toxicity. Here, we present a metabolomic investigation of a coculture of liver sinusoidal endothelial cells (LSECs, SK-HEP-1) with hepatocytes (HepG2/C3a) using advanced organ-on-chip technology. To reproduce the physiology of the sinusoidal barrier, LSECs were separated from hepatocytes by a membrane (culture insert integrated organ-on-chip platform). The tissues were exposed to acetaminophen (APAP), an analgesic drug widely used as a xenobiotic model in liver and HepG2/C3a studies. The differences between the SK-HEP-1, HepG2/C3a monocultures and SK-HEP-1/HepG2/C3a cocultures, treated or not with APAP, were identified from metabolomic profiles using supervised multivariate analysis. The pathway enrichment coupled with metabolite analysis of the corresponding metabolic fingerprints contributed to extracting the specificity of each type of culture and condition. In addition, we analysed the responses to APAP treatment by mapping the signatures with significant modulation of the biological processes of the SK-HEP-1 APAP, HepG2/C3a APAP and SK-HEP-1/HepG2/C3a APAP conditions. Furthermore, our model shows how the presence of the LSECs barrier and APAP first pass can modify the metabolism of HepG2/C3a. Altogether, this study demonstrates the potential of a “metabolomic-on-chip” strategy for pharmaco-metabolomic applications predicting individual response to drugs.

Keywords: organ-on-chip, LSECs, hepatocytes, coculture, metabolomic, acetaminophen

1. Introduction

Toxicological evaluation of a substance is usually achieved through the combined use of several types of experimental models, including *in vitro* cell culture models, *in vivo* animal models, and *in silico* computer simulations which make it possible to predict biochemical interactions between the organism and a chemical substance (Guillouzo, 1998; Bhushan et al., 2016; Caloni et al., 2022). However, animal models display different responses compared to humans and raise ethical issues, while conventional *in vitro* cultures are poorly representative of human *in vivo* physiology, metabolism and toxicity (Ruoß et al., 2020).Therefore, the development of novel *in vitro* methodologies, including fast and effective screening tools to predict individual toxicity of chemical compounds, is of prime interest in the context of international regulations, such as the European registration, evaluation, authorization and restriction of chemical substances (REACH) which requires any substance to be evaluated for possible risks to humans, animals, or the environment (Caloni et al., 2022; Rim, 2020; Tsaioun et al., 2016).

Among the advanced *in vitro* methods, organ-on-chip is a technology that has emerged from the combination of microelectronics, tissue engineering and biomaterial sciences (Messelmani et al., 2022a). An organ-on-chip consists in a miniaturized tissue culture system that makes it possible to create and maintain 3D organs on a small scale, as well as engineering dynamic conditions, and which reproduces some of the key *in vivo* features within a well-controlled environment (see example for liver in Messelmani et al., 2022a; Moradi et al., 2020; Dalsbecker et al., 2022). In this context, our team has built an organ-on-chip platform for the coculture in 3D of liver tissues with barrier models to investigate organ-to-organ interactions (intestine-liver, Bricks et al., 2014; liver- testis, Zeller et al., 2017), and first pass metabolism of drugs (Bricks et al., 2015). The platform was recently used to investigate the coculture of a liver sinusoidal endothelial cell barrier with hepatocyte biochip. Then, the technology was applied to the acetaminophen passage through the sinusoidal-like barrier and the subsequent metabolism by the hepatic cells (Messelmani et al., 2023).

In parallel to these technological developments, our group proposes a “metabolomic-on-chip” approach combining organ-on-chip technologies with metabolomic analyses. Metabolomic analyses relate to the untargeted identification of low-molecular weight compounds (metabolites < 1500 Da) present in a biological system and variations in concentrations in response to a pathophysiological

perturbation or genetic modifications (Canzler et al., 2020; Dufour-Rainfray et al., 2020; Jellali et al., 2021). Metabolic phenotyping studies can be used as a tool for understanding the metabolic modifications after exposure to a substance (Song et al., 2016). Analytical spectroscopic methods, such as nuclear magnetic resonance (NMR) spectroscopy and mass spectrometry (MS), make it possible to detect and quantify metabolites in various samples from biofluids such as serum or urine, as well as cells and tissues (Duarte and Gil, 2012; Agin et al., 2016). We previously characterized organ-to-organ communications (such as liver and testis, Zeller et al., 2017, liver-kidney, Shintu et al., 2012) and the effects of several molecules (including drugs, solvents, pesticides) in liver organ-on-chip models populated with HepG2/C3a cells (Shintu et al., 2012), with rat primary hepatocytes (Jelalli et al., 2018) and islets of Langerhans (Essaouiba et al., 2022).

To improve knowledge on the interactions between liver sinusoids and hepatocytes, we suggested characterizing their crosstalk using the metabolomic-on-chip approach in our coculture platform using LSECs-HepG2/C3a. Then, we extended the analysis to the tissue crosstalk during an acetaminophen treatment. Acetaminophen was selected as the primary model compound because it is a widely used antipyretic and analgesic treatment which has also been studied extensively. Furthermore, APAP overdose is a well-recognized cause of hepatotoxicity (Shen at al., 2006) and cytotoxicity (Milam and Byard, 1985). APAP is essentially metabolized in the liver, and major phase 2 detoxification pathways are sulphate and glucuronic acid conjugations. Acetaminophen is mainly excreted in urine as glucuronide (APAP-G) and sulphate (APAP-S) metabolites in humans and rats. However, a minor phase 1 metabolic pathway leads to the formation of a toxic intermediary, *N*-acetyl-*p*-benzoquinone-imine (NAPQI, Dahlin et al., 1984). This intermediary can cause delayed and irreversible liver lesions (Reid et al., 2005). NAPQI can be retro-converted to the APAP glutathione conjugate (APAP-GSH) through glutathione-S-transferase activity, which can later produce cysteine and *N*-acetylcysteine conjugates (APAP-CYS and APAP-NAC, respectively). The metabolomic profiles of our HepG2/C3a liver-on-chip, with and without APAP exposure, have been previously characterized and compared to static Petri culture (Ouattara et al., 2012; Prot et al., 2012; Shintu et al., 2012).

In the present study we extended this analysis using SK-HEP-1 cells as a LSECs barrier to reproduce a more physiological situation mimicking liver APAP penetration

from the sinusoids to the hepatocytes. For this purpose, we firstly investigated the crosstalk between the HepG2/C3a and SK-HEP-1 tissues. Then, we exposed the SK-HEP-1 to APAP to investigate the changes in the metabolome illustrating HepG2/C3a and SK-HEP-1 tissue interactions.

2. Materials and methods

2.1. Cells and culture medium

HepG2/C3a (LGC standards, ATCC-CRL-10741) and SK-HEP-1 cells (LGC standards, ATCC-HTB-52) were used as hepatocyte and LSECs models, respectively. The cells were cultured in a mixture of 75% Minimal Essential Medium MEM with phenol red (Pan Biotech), 25% of Endothelial cell Growth Medium 2 EGM-2 (Lonza, CC-3162) according to previous optimization (Messelmani et al., 2023). MEM was supplemented with 10% foetal bovine serum (Gibco), 1 mM hydroxy-ethylpiperazine-N-2-ethanesulfonic acid HEPES (Gibco), 2 mM L-glutamine (Gibco), 0.1 mM non-essential amino acids (Gibco), 1 mM sodium pyruvate (Gibco), and 100 U/mL penicillin, 100 µg/mL streptomycin (Pan Biotech). Cells were cultured in 75 cm^2 flasks at 37 °C in a humidified atmosphere with 5% CO_2. The culture medium was renewed every 2 days and the cells were passaged weekly when reaching 80-90% confluence. The cells were detached between passages 10 and 20 using trypsin-EDTA 0.25% (Gibco) for use in the experiments.

2.2. Biochip fabrication

The details of the biochip design and manufacturing process were reported in a previous work (Jellali et al., 2016). Briefly, the biochip consists of two polydimethylsiloxane PDMS layers (Dow Corning, Sylgard 184 kit) manufactured by soft lithography and sealed via plasma treatment. To promote 3D cell organization, a hyaluronic acid (HA)-based hydroscaffold (RGDS-grafted HA, galactosamine-grafted HA, collagen type I and collagen type IV) was integrated into the biochip (HCS Pharma, BIOMIMESYS® Liver). The pseudo-hydrogel solution containing HA, collagen and crosslinker (adipic acid dihydrazide) was injected into the biochip and the hydroscaffold crosslinking was performed *in situ*. The biochips were then washed with distilled water,

freeze-dried, and sterilized by ultraviolet exposure. The detailed protocol and device characterization were previously described (Messelmani et al., 2022b).

2.3. Dynamic monoculture and coculture

2.3.1. IIDMP fluidic platform

The IIDMP (Integrated Insert in a Dynamic Microfluidic Platform) fluidic platform used for making a SK-HEP-1 barrier and HepG2/C3a biochip coculture or monoculture was extensively described by Bricks et al., (2014). The platform, made of polycarbonate, was manufactured to include three cell culture inserts and three biochips. Therefore, each IIDMP was composed of three independent coculture units. Each coculture unit was composed of the association of an insert and a biochip linking two wells (Fig.1A). The insert was placed in the first well and defined an apical pole (the LSECs barrier) and a basal pole making possible the exchange of culture medium between the LSECs barrier and the hepatocyte compartment (biochip). The biochip connected the first and second well, acting as a reservoir. The total volume of culture medium was 10 mL: 1 mL in the apical insert, 5 mL below the insert, and 4 ml in the second well. To make recirculating perfusion possible, the second well and the basal compartment of the first well were connected to a peristaltic pump using a specific lid which hermetically closed the platform.

2.3.2. Experimental procedure of cultures

The detailed experimental procedure is presented in Fig.1B. First, SK-HEP-1 cells were seeded in culture inserts with polyethylene terephthalate membrane and 0.4 µm of porosity (Greiner, THINCERT 6-well format,) at a density of 0.35 10^5 cells/cm^2. The culture medium was renewed every 2 days in the apical (1 mL) and basal (2 mL) compartments. The culture was maintained in static condition until confluence was attained, forming a homogenous barrier (8 days, Messelmani et al., 2023). Then, 24 h before the dynamic experiments, HepG2/C3a cells were seeded in the biochips (4 10^5 cells/biochip) and incubated in static condition overnight at 37 °C in a humidified atmosphere with 5% of CO_2.

On Day 0, the SK-HEP-1 inserts and HepG2/C3a biochips were connected to the IIDMP platform, and the culture medium was added (1 mL in the apical insert side, 5 mL in the basal side and 4 mL in the reservoir well). When indicated, acetaminophen APAP (Sigma-Aldrich) was loaded into the apical compartment of the LSECs insert at 1 mM (an insert without cells was used for HepG2/C3a monoculture experiments). After dilution in the total medium in the circuit (10 mL), the systemic concentration of APAP was 100 µM. Then, the IIDMP was closed and connected to the peristaltic pump. The entire setup was placed in the incubator and perfusion started at 10 µL/min for 48 h in a closed loop.

For comparative purposes, we compared the SK-HEP-1/HepG2/C3a dynamic cocultures (in the IIDMP platform) results with SK-HEP-1 and HepG2/C3a monocultured in the IIDMP. For SK-HEP-1 dynamic monocultures, the LSECs inserts were connected to the biochip without cells in the platform. HepG2/C3a monocultures were done by running the IIDMP platform containing the HepG2/C3a biochip and insert without cells.

2.4. Immunostaining assays

The nuclei, F-actin, PECAM-1 and stabilin-2 stainings were performed using cells fixed in phosphate buffered saline PBS (Gibco), 4% paraformaldehyde (MP biomedicals) and permeabilized with PBS, 1% Triton X100. SK-HEP-1 inserts were incubated in mouse anti-PECAM-1/CD31, 1 µg/mL (abcam, ab24590) and rabbit anti-stabilin-2, 1 µg/mL (abcam, ab121893) primary antibodies overnight at 4 °C. After washing, the samples were further incubated with donkey anti-mouse Alexa Fluor 647, 2 µg/mL (abcam, ab150107) and goat anti-rabbit Alexa Fluor 488, 2 µg/mL (Invitrogen, A11034) overnight. The nuclei and actin cytoskeleton (SK-HEP-1 and HepG2/C3a) were stained using Alexa Fluo 488 Phalloidin 1/50 (Thermo Fisher) for 3h and 4′,6-diamidino-2-phenylindole DAPI 10 µg/mL (Invitrogen, D1306) for 30 min, respectively. Imaging was performed using a Zeiss LSM 710 laser scanning confocal microscope.

2.5. HepG2/C3a functionality

Albumin and urea secreted by HepG2/C3a cells was quantified using a human albumin ELISA Quantitation Set (Bethyl Laboratories, E80-129) and QuantiChrom urea

assay (BioAssay Systems, DIUR-100), respectively. The results were obtained with a Spectafluor Plus microplate reader (TECAN) set to a wavelength of 450 for albumin and 520 nm for urea.

The analyses were performed with 6 replicates from three independent experiments (n = 6) and the data are presented as the mean ± SD. One-way ANOVA was performed for statistical analysis (GraphPad Prism 8 software, State College, USA) and a *P* value less than 0.05 was considered as statistically significant.

2.6. Metabolomic analyses

2.6.1. Gas chromatography coupled to mass spectrometry (GC-MS) analyses

The metabolomic analyses were performed on the culture media collected at the end of the experiments. For each culture condition, five samples from three independent experiments were used (n = 5). Sample preparation and metabolite extraction were performed according to our previous work (Jellali et al., 2020). Briefly, 250 µL of culture medium were mixed with 500 µL of extraction solution (-20 °C) of water:acetonitrile:isopropanol (2:3:3) containing 4 mg/L of ribitol, 2.75 mg/L of α-aminobutyric acid solution αABA, and stirred in an Eppendorf thermomixer (1500 rpm) for 10 min at 4 °C. Insoluble material was removed by two centrifugations steps at 14000 rpm for 15 min. Then, the samples were dried for 4 h at 35 °C in a speed-vac and stored at -80 °C until analysis.

Before GC-MS injection, samples were dried again for 2 h and 10 µL of methoxyamine solution in pyridine (20 mg/mL) were added. After 90 min at 30 °C, 90 µL of N-methyl-N-trimethylsilyl-trifluoroacetamide MSTFA (Regis Technologies) were added and the reaction continued for 30 min at 37 °C. Finally, 100 µL of solution was transferred to an Agilent vial for injection. Four hours after derivatization, 1 µL of sample was injected in splitless mode on an Agilent 7890B gas chromatograph (Agilent, Santa Clara, USA) coupled to an Agilent 5977A quadrupole mass spectrometer. The column was a Rxi-5SilMS (30 m with 10 m Integra-Guard column) from Restek (Lisses, France). An injection in split mode with a ratio of 1:30 was systematically performed for saturated compound quantification. The oven temperature ramp was 60 °C for 1 min then 10 °C/min to 325 °C for 10 min. Helium constant flow was 1.1 mL/min. Temperatures were the following: injector: 250 °C, transfer line: 290 °C, source: 230 °C

and quadrupole 150 °C. The quadrupole mass spectrometer was switched on after a 5.90 min solvent delay time, scanning from 50-600 u. Samples were randomized and a fatty acid methyl ester mix (C8, C9, C10, C12, C14, C16, C18, C20, C22, C24, C26, C28, C30) was injected in the middle of the queue for external RI calibration.

Raw Agilent data files were analysed with AMDIS (www.amdis.net). The Agilent Fiehn GC/MS Metabolomics RTL Library (version June 2008) was employed for metabolite identifications. Peak areas were determined with the Masshunter Quantitative Analysis (Agilent) in splitless and split 30 modes. Because automated peak integration was occasionally erroneous, integration was verified manually for each compound and peak areas were normalized to ribitol. Metabolite contents are expressed in arbitrary units (semi-quantitative determination).

2.6.2. Metabolomic statistical analyses

The metabolomic multivariate data analyses were performed using MetaboAnalyst 5.0 (Pang et al., 2021). Before analysis, a pre-treatment was applied to GC-MS data: autoscaling, the most known pre-treatment methods in metabolomics (Gromski et al., 2015). Firstly, unsupervised principal component analysis (PCA) was performed to identify the similarity or the differences between sample profiles and to assess the clustering behavior between groups. Then, supervised partial least squares-discriminant analysis (PLS-DA, comparison of more than two groups) and orthogonal projections to latent structures discriminant analysis (OPLS-DA, comparison of two groups) were applied to get the maximum separation between control and treated groups, and to explore the variables that contributed to this separation. The quality of PLS-DA and OPLS-DA models was evaluated by the R^2Y (fitting degree) and Q^2 (prediction parameter) values. To determine the best discriminator metabolites, the P value (Student's t-test) and fold change were used to build the volcano plot -log10P = f (log2FC). Variables with P value < 0.05 and fold change > 1.2 (upregulated) or < 0.8 (down regulated) represent possible discriminating metabolites. The significant metabolites were confirmed using variable importance in the projection value (VIP > 1). Finally, pathway enrichment analysis was performed with MetaboAnalyst using the selected significant metabolites.

3. Results

3.1. Morphology and functional characterization of the tissues

The SK-HEP-1 cells were cultured in static inserts until the formation of a confluent and homogenous LSECs barrier (8 days). Then, they were cultured in dynamic conditions for two days, with or without APAP exposure. The SK-HEP-1 morphology at the end of the experiments, in monoculture and coculture (control and exposed to APAP), is presented in Fig.2A. SK-HEP-1 cells were able to form and maintain a confluent and continuous barrier constituted of several cell layers. Actin staining confirmed the development of the microfilament cytoskeleton in all cells across the whole insert surface, and the formation of different cell layers (Fig.2B and 2C, examples of z-stack performed using confocal microscopy in Fig.S1). However, compared with SK-HEP-1 monoculture, the actin network was composed of more elongated filaments in the coculture. Under APAP exposure, the actin cytoskeleton seems to be composed of elongated and disorganized filaments, both in monoculture and in coculture. Finally, SK-HEP-1 monocultures and cocultures without APAP were positive to the LSECs specific marker PECAM-1 and stabilin-2 (Fig.2B). Conversely, PECAM-1 and stabilin-2 signal intensities was reduced in SK-HEP-1 cultures exposed to APAP, especially in coculture condition (Fig.2C).

In the biochips, the HepG2/C3a cells attached to the hydroscaffold and aggregated in small clusters of cells after 24 h in static conditions (Fig.3A). Then, the biochips were connected to the fluidic platform and monocultured or cocultured with SK-HEP-1 barrier for 48 h. As for SK-HEP-1 cells, we did not detect any difference in the HepG2/C3a morphologies at the end of the experiments, when compared the HepG2/C3a monocultures, the SK-HEP-1/HepG2/C3a cocultures without or with APAP. After 48 h in dynamic cultures, the cells proliferated and formed large aggregates/spheroids in all culture conditions (Fig.3B). Actin formed a complex filament network across the whole spheroids, without any significant difference between monocultures and cocultures (with and without APAP, Fig.3C and 3D).

The hepatic functionality of the HepG2/C3a was confirmed by measuring the secretion of albumin and urea. As shown in Table 1, the HepG2/C3a monocultures and cocultures treated or not with APAP secreted similar quantities of albumin (secretions ranging between 114 ± 16 and 129 ± 27 ng/h). Finally, urea production was measured

in HepG2/C3a monoculture and SK-HEP-1/HepG2/C3a coculture (Table 1). Without APAP treatment, the secretion of urea was higher in HepG2/C3a monoculture (2.14 ± 0.44 µg/h), than in coculture (1.19 ± 0.16 µg/h). In the cultures exposed to APAP, the urea secretion was significantly decreased, both in monoculture (4-fold lower than monoculture without APAP) and in coculture (2-fold lower than coculture without APAP).

3.2. Identification of the HepG2/C3a, SK-HEP-1 and SK-HEP-1/HepG2/C3a specific metabolomic signatures

At the end of the experiments, the supernatants from the different culture conditions were collected and analysed with gas chromatography coupled to mass spectrometry (GC-MS). The analysis led to the identification of 94 metabolites (Table S1, supplementary file 1). To identify the metabolomic signature of each culture mode without APAP exposure, we performed a multivariate analysis (unsupervised PCA and supervised PLS-DA) using the metabolomes of SK-HEP-1 monoculture, HepG2/C3a monoculture, SK-HEP-1/HepG2/C3a coculture and basal culture medium. The PCA analysis could not sufficiently separate the groups (Fig.S2, supplementary file 1). No significant differences between SK-HEP-1 monoculture, HepG2/C3a monoculture and SK-HEP-1/HepG2/C3a coculture were revealed in the PCA. Only medium samples were clearly separated from the samples of different cultures. The PLS-DA score plots showed a clear separation between the three culture modes and basal medium, indicating distinct metabolic profiles (Fig.4A). The distance between HepG2/C3a monoculture and coculture groups was weak due to the closer metabolic profiles of these modes compared to the others. The PLS-DA analysis (VIP > 1) coupled to the ANOVA test (*P* value < 0.05) identified 58 metabolites. The heatmap of the top 40 significant metabolites is given in Fig.4B. The detailed heatmap with the 58 metabolites is presented in Fig.S3 and the full list of the 58 metabolites with the corresponding *P* value in Table S2 (supplementary file 1).

The specific signature of the HepG2/C3a monoculture was characterized by the high production of urea, ornithine, glycine, iminodiacetic acid and glycerol-1-phosphate, and the high consumption of glycerol and pantothenic acid. The HepG2/C3a cells displayed moderate lipid synthesis including caprylic, capric, hexanoic, oleic and palmitoleic acids, when compared to SK-HEP-1 and the cocultures. There was also a

weak production of the pentose phosphate metabolites (ribose, arabinose) and a moderate consumption of glucose, fructose, allose and pyruvic acid, coupled to moderate lactate production, when compared to other conditions.

The SK-HEP-1 monoculture produced the highest levels of palmitoleic acid, oleic acid, ribose, arabinose, galactitol, hypoxanthine and 2,3 butanediol. Overall, the SK-HEP-1 cells were characterized by high lipid synthesis (oleic, palmitoleic, capric, caprylic, and hexanoic acids), an active pentose phosphate pathway (high ribose and arabinose secretion) and intense polyol metabolism highlighted by the high consumption of mannitol, xylitol, sorbitol, and threitol, when compared to HepG2/C3a monocultures). The LSECs culture metabolome revealed high consumption of glucose, tagatose, and fructose, associated with lactic acid production, suggesting intense glycolysis activity compared to HepG2/C3a monoculture. Finally, there was production of tricarboxylic acid TCA cycle intermediates: succinic, alpha ketoglutaric, malic, and citric acids, in comparison with the basal medium.

The SK-HEP-1/HepG2/C3a coculture presented a signature in synergy with the HepG2/C3a and SK-HEP-1 monocultures. The HepG2/C3a monocultures and the cocultures presented a common signature, including high levels of alanine, 2-ketoisocaproic acid, benzoic acid, glycerol 1 phosphate, and glutamic acid, and low levels of pantothenic acid, succinic acid, and glycerol. The common metabolites highlighted by SK-HEP-1 monocultures and SK-HEP-1/HepG2/C3a cocultures included high levels (production) of oleic acid, palmitoleic acid, lactic acid, ribose, arabinose, and asparagine, and low levels (consumption) of myo-inositol, citraconic acid, carbohydrates (mannitol, allose, fructose, glucose, sorbitol, threitol, and xylitol), threonine, serine, ethanolamine and beta-alanine.

Finally, all three culture conditions (SK-HEP-1 monocultures, HepG2/C3a monocultures and cocultures) presented several common signatures, such as the production of capric acid, hexanoic acid, caprylic acid, lactic acid, alpha ketoglutaric acid, malic acid, ornithine, and 3-methyl-2-oxobutaric acid. In parallel, high consumption of amino acids (isoleucine, methionine, threonine, glutamine, citrulline and phenylalanine), pyridoxine, glucose-6 phosphate, and 4-hydroxyproline was observed.

3.3. Metabolomic signature of APAP exposure

PCA analysis was applied to the overall dataset to compare the metabolic profiles of cultures exposed to APAP, cultures without APAP and medium. The PCA score plots highlighted three separate groups: medium samples, SK-HEP-1 monoculture exposed to APAP and the third group consisting of all other samples (Fig.S4, supplementary file 1). The PLS-DA analysis made possible better separation between the different culture modes and the basal medium (Fig.S5, supplementary file 1). However, the distance between the cultures treated or not with APAP was weak (with overlap between the two groups). Furthermore, the PLD-DA model reveled a poor fitting degree (R^2 = 0.6) and predictability (R^2 = 0.39).

3.3.1. Effect of APAP on the HepG2/C3a monoculture

To identify potential biomarkers and the effects of APAP exposure on HepG2/C3a monocultures, a supervised OPLS-DA analysis was applied to the metabolomes of HepG2/C3a control and APAP treated HepG2/C3a. As shown in the OPLS-DA score plot (Fig.5A), the analysis played a part in clearly identifying cultures treated or not with APAP, indicating significant differences between the two metabolomes. To extract the biomarkers, a volcano plot was drawn using the *P* value (-log10P) and fold change (log2FC). The volcano plot revealed 13 metabolites modulated by APAP exposure ($P < 0.05$): 2 downregulated (FC < 0.8) and 11 upregulated (FC > 1.2; Fig.5B and C). The full statistical analysis, including all metabolites, *P* value, FC and VIP, is provided in supplementary file 2.

The effect of APAP on HepG2/C3a cultures was characterized by the specific over production of glycolic acid, ribose, arabinose, hypoxanthine, tyrosine, leucine, and glycerol-1-phosphate, when compared to the HepG2/C3a control. APAP increased the consumption of mannitol, and reduced both the production of sucrose and the consumption of glucose-6-phosphate. Finally, valine and cystine levels were higher in cultures exposed to APAP when compared to the control, indicating a lower consumption or a change in the production/consumption balance. The pathway enrichment analysis with the metabolites discriminating HepG2/C3a control and HepG2/C3a exposed to APAP highlighted the pentose phosphate pathway, starch and

sucrose metabolism, and galactose metabolism ($P < 0.05$).(Fig.5D). The complete analysis is provided in supplementary file 2.

3.3.2. Effect of APAP on the SK-HEP-1 monoculture

The OPLS-DA analysis performed with the SK-HEP-1 control and APAP exposed SK-HEP-1 samples successfully separated both groups with a high quality of fit and predictability ($R^2 = 0.84$, $Q^2 = 0.74$; Fig.6A). The volcano plot construction made it possible to extract 26 metabolites (P value < 0.05 and VIP > 1) significantly modulated in SK-HEP-1 exposed to APAP: 4 downregulated FC < 0.8 and 22 upregulated FC > 1.2 (Fig.6B and 6C). The full statistical analysis (P value, FC and VIP scores) is presented in supplementary file 3.

The heatmap in Fig.6C shows that the APAP treatment reduced the consumption of citrulline, fructose and pyruvic acid, and the production of hexanoic acid and galactitol. In parallel, compared to SK-HEP-1 control cultures, APAP treatment increased the production of asparagine, leucine, creatinine, ornithine, cysteine, glycolic acid, lipids and fatty acids (glycerol, glycerol-1-phosphate, myristic acid, palmitic acid, and lauric acid), TCA cycle substrate (fumaric acid), xanthine and uric acid (purine metabolism). Finally, the pentose carbohydrate (arabinose and ribose), melibiose, pyroglutamic acid, and oxalic acid secretions also increased in SK-HEP-1 exposed to APAP when compared to the SK-HEP-1 control. The pathway enrichment analysis using the metabolites differentially expressed between SK-HEP-1 cultures with and without APAP revealed that urea cycle, fatty acid biosynthesis, galactose metabolism, glycerolipid metabolism and glycine, and serine metabolism were the top 5 enriched pathways. Of the top 10 pathways, we also found aspartate metabolism and beta oxidation of very long chain fatty acids ($P < 0.05$, Fig.6D, complete analysis in supplementary file 3).

3.3.3. Effect of APAP on the SK-HEP-1/HepG2/C3a cocultures

Metabolomic profiling was also performed on the SK-HEP-1 barrier cocultured with the HepG2/C3a biochip and exposed to APAP. Fig.7A shows the OPLS-DA score plot from multivariate analysis performed with the metabolome of control and APAP treated coculture. Clearly, the OPLS-DA score plot shows significant separation of the

two groups in distinct clusters (R^2 = 0.82, Q^2 = 0.7). In total, 27 metabolites were modulated by APAP treatment (P < 0.05), with 6 and 21 metabolites downregulated (FC < 0.8) and upregulated (FC > 1.2), respectively (volcano plot and heatmap in Fig.7B and 7C). The results of the full statistical analysis are provided in supplementary file 4.

The coculture exposed to APAP exhibited notable high production of oxalic acid, proline, ornithine, glutamic acid, TCA cycle intermediates (fumaric acid, citric acid and malic acid), alpha ketoglutaric acid, 2-ketoisocaproic acid, asparagine, threonic acid, cysteine, leucine and glycerol-1 phosphate. Compared to the control coculture, APAP exposure increased the consumption of phenylalanine, methionine, isoleucine and succinic acid. Conversely, the consumption of pyridoxine, deoxyglucose, threitol and mannitol was reduced by APAP treatment. The pathway enrichment analysis highlighted valine, leucine and isoleucine degradation, the urea cycle, arginine and proline metabolism, the malate-aspartate shuttle, phenylalanine and tyrosine metabolism, the Warburg effect and citric acid cycle among the top enriched pathways (P value < 0.05, Fig.7D). The full analysis is presented in supplementary file 4.

3.3.4. Common and specific biomarkers of three cultures exposed to APAP

To elucidate the common and specific signatures of each culture condition after APAP treatment, a Venn diagram was designed using the biomarkers of three culture conditions: SK-HEP-1 monoculture, HepG2/C3a monoculture and SK-HEP-1/HepG2/C3a coculture. As shown in Fig.8 and Table S3, three biomarkers were common to the SK-HEP-1 and HepG2/C3a monocultures, two to the coculture and HepG2/C3a monocultures, six to the coculture and SK-HEP-1 monocultures, and three to all three conditions. After exposure to APAP, the three culture conditions presented a common signature, including high production of asparagine, glycerol 1-phosphate and leucine. Among the metabolites common to the SK-HEP-1 monoculture and coculture exposed to APAP, we found increased secretion of fumaric acid, pyroglutamic acid, ornithine, oxalic acid and cysteine, and consumption of methionine. Finally, the common metabolites highlighted by the SK-HEP-1 and HepG2/C3a monocultures treated with APAP included higher production of glycolic acid arabinose and ribose, whereas sucrose and mannitol were common biomarkers to HepG2/C3a monocultures and coculture.

4. Discussion

In this study, metabolomic profiling was used to investigate the effect of APAP on LSECs-hepatocyte coculture, and the crosstalk between the two cell types. Organ-on-chip technology coupled to the use of a hydroscaffold mimicking the liver ECM made it possible to culture hepatocytes (HepG2/C3a) in a complex 3D dynamic configuration. To mimic the physiology of the liver sinusoid, the HepG2/C3a biochip was cocultured with a LSECs barrier (the SK-HEP-1 cell line cultured on a membrane insert). The LSECs-hepatocyte paracrine-like communication was made possible by exchanges through the insert membrane and the dynamic culture in a microfluidic platform. Characterizing the coculture confirmed that both cell types maintained their typical morphologies and functionalities. We also demonstrated APAP transit through the LSECs barrier to the liver biochip compartment (Table 1, Messelmani et al., 2023). The metabolomic analyses contributed to extracting a common signature and specific patterns in the culture conditions tested.

4.1. Identification of the specific metabolic signatures from mono to cocultures

The metabolomic analyses revealed a synergy in metabolic profiles between the cell types when they are cultured together. First, comparing the culture medium of the SK-HEP-1 monocultures, HepG2/C3a monocultures, SK-HEP-1/HepG2/C3a cocultures and basal culture medium illustrated clear differences between the culture conditions. The SK-HEP-1 monocultures were characterized by cellular activity in the polyol pathway, in the pentose phosphate pathway, intense glycolysis and TCA cycle activation. Under healthy conditions, endothelial cells rely on glycolysis on an energy source (Pi et al., 2018). They divert into a polyol pathway due to high glucose concentration medium (Oyama et al., 2006; Pi et al., 2018). Our signature may reflect a probably too high glucose concentration and potential LSECs culture medium optimization. We also detected intense lipid synthesis. Endothelial cells produced fatty acids to feed vascular sprouting (Wong et al., 2017) and high glucose did not seem to particularly affect their lipid secretion (Duhault et al., 1979).

In comparison, in the HepG2/C3a monoculture, we found no specific activation of the polyol pathway, moderate activation of the pentose phosphate pathway (PPP), glycolysis and consistently of the TCA cycle. We also found moderate lipid synthesis.

HepG2/C3a were characterized by a high glycerol metabolism. Interestingly, the coculture included a synergy of both SK-HEP-1 and HepG2/C3a metabolism. As such, in cocultures, we found activation of the polyol pathway, pentose phosphate pathway, and intense glycolysis activation coupled with TCA cycle activation, similar to the SK-HEP-1 monocultures. We also detected significant lipid synthesis.

Then, consistently with HepG2/C3a monocultures, the coculture signature included intense glycerol metabolism, and alanine, benzoic acid, 2-ketoisocaproic acid and glutamic acid production when compared to SK-HEP-1. Interestingly, 2-ketoisocaproic acid (degradation of leucine) is associated with production of diacyglycerol in hepatocytes (Yagasaki et al., 2002), which appeared consistent with the glycerol metabolism in our data. In parallel, benzoic acid metabolism is reported to reflect the mitochondrial functions in rat hepatocytes (Krahenbul et al., 1997), which may reflect oxidative phosphorylation in the HepG2/C3a cells.

4.2. Identification of APAP metabolic perturbation in HepG2/C3a

In our previous work using a HepG2/C3a liver-on-chip, we identified a toxic metabolomic signature of APAP after exposure at 1 mM for 96 h which was associated with cell death. Among the metabolites, this toxic signature was characterized by the production of pyroglutamic acid, 2-hydroxybutyric acid, 3-hydroxybutyric acid, serine, proline, alanine and lactate (Prot et al., 2012). The kinetics analysis of the exposure of 1 mM of APAP for 24h to 144 h in a HepG2/C3a liver-on-chip was associated with the induction of reactive oxygen species (ROS) at 72h of exposure (Leclerc et al., 2015). This ROS expression was correlated with extensive GSH depletion after 48h of culture, reduction of cell proliferation after 72h of exposure, and with cell toxicity after 96h of exposure, especially above 0.5 mM (Leclerc et al., 2015).

The present exposures were performed at 1 mM in the LSECs insert, resulting in a systemic APAP concentration of 100 µM (HepG2/C3a exposure for 48h). The condition used here did not lead to specific cell death, nor to HepG2/C3a inflammation, consistently with our previous work (no IL-6 nor TNFα secretion, Messelmani et al., 2023). The lack of toxicity could also be explained by the 3D organization of the cells (in contrast to the 2D cultures reported in Prot et al., 2012 and Leclerc et al., 2015). Mueller et al., (2014) demonstrated that HepG2/C3a spheroids were more resistant to drugs than 2D cultures. Furthermore, in the present metabolomic signature, we did not

detect the element of the metabolites associated with HepG2/C3a cell death in biochips (Choucha Snouber et al., 2013; Prot et al., 2012), nor typical APAP toxicity biomarkers such as 5-oxoproline/pyroglutamamic acid, a typical drug-induced liver injury biomarker (Lu, 1999; Yang et al., 2012; Lord and Bralley, 2008), hippuric acid (Schnackenberg et al., 2017) and ROS biomarkers (Gall et al., 2010). Nevertheless, the present APAP-treated HepG2/C3a signature was characterized by high levels of glycolic acid. This compound is a natural antioxidant molecule that reduces reactive oxygen species-induced cell death (Diez et al., 2021). Detecting this compound may reflect an early response to the APAP stress.

In the present experiments, we detected changes in carbohydrate homeostasis and a glycolytic switch, as we detected activation of the pentose phosphate pathway (accumulation of ribose and arabinose, low production of sucrose and consumption of mannitol). As APAP disrupts mitochondrial functions and oxidative phosphorylation (Jaeschke et al., 2019), APAP poisoning leads to disrupted aerobic respiration (Shah et al., 2011). Overall, we observed the onset of the effects of APAP illustrated by the hallmarks of early but weak hepatotoxicity (respiration switch), however the signature did not present either cell death markers or strong inflammation propagation. Furthermore, one natural molecule involved in the cell defence mechanism was detected.

4.3. Identification of APAP metabolic perturbation in SK-HEP-1 monocultures

APAP was reported to induce LSECs death *via* the TRAIL (TNFα) pathway (Badmann et al., 2012). It was also reported that TRAIL apoptosis alters lipid mitochondrial homeostasis, including the phosphocholine and diacylglycerol (DAG) balance, leading to caspase 8 activation (Ferry et al., 2005). In our study, APAP did not lead to significant TNFα release in LSECs monocultures (Messelmani et al., 2023), but it contributed to increasing the glycerol and glycerol-1-phosphate that are metabolites involved in DAG production. We also detected high lipid production, illustrated by the high levels of palmitic, lauric and myristic acids. Interestingly, it was reported that lipids promoted LSECs survival, proliferation, and the maintenance of the differentiation in rat *in vitro* cell cultures (Hang et al., 2012). However, high levels of palmitic acid supplementation played a part in damaging LSECs fenestration and modifying molecule clearance (Cogger et al., 2016). Furthermore, the excess of

palmitic acid is widely reported in the literature as a source of cell death, including in LSECs (Geng et al., 2020). Although we detected the production of pyroglutamic acid (an ROS production biomarker), we did not detect such cell death in our experiments and additional assays are required to address this point.

SK-HEP-1 treatment with APAP increased the accumulation of ornithine, creatinine and citrulline in the medium. Arginine is synthetized using glutamic acid as a substrate (Li et al., 2022). Then, arginase is a key enzyme degrading arginine to ornithine and urea (Li et al., 2022). However, under nitric oxide synthase (NOS), arginine can also be degraded into citrulline and nitric oxide (NO). Urea is excreted as the final product, whereas ornithine is recycled for polyamine synthesis (Li et al., 2022). Therefore, we observed potential arginine metabolism modulation in our LSECs cultures when treated with APAP. Although NO is very important in LSECs function (Xie et al., 2012; Wang and Peng, 2021), an over production of NO (due to NOS) leads to LSECs toxicity and even liver disorders (Iwakiri and Kim, 2015; Wang and Peng, 2021). Interestingly, the increases in fatty acid and TNF activation are reported to increase NO activity and then cell stress in liver (Stanimirovic et al., 2015).

Finally, the APAP signature modified carbohydrate metabolism and the TCA cycle in SK-HEP-1 monocultures. We observed repression of the glycolysis pathway *via* weaker pyruvate and fructose consumptions, and an accumulation of arabinose and melibiose. Furthermore, the pentose phosphate pathway (PPP) appeared active, as shown by the production of ribose and arabinose, illustrating a glycolysis switch. The switch was concomitant with the accumulation of the TCA cycle substrate, fumaric acid. Although excess arabinose is reported to open tight junctions in endothelial brain cells (Dorovini-Zis et al., 1984), it has also been reported as repairing tight-junction proteins in the brain and providing protection against inflammatory cytokine-induced endothelial permeability by down regulating NF-κB signals (Li et al., 2021). Furthermore, low levels of glycolysis in LSECs were associated with the inflammation process (IL-6 stimulated inflammation, Dudek et al., 2022). PPP activation with a glycolysis switch was reported in neutrophils as a defence mechanism to suppress oxidative burst (Britt et al., 2022). In parallel, as in the HepG2/C3a monoculture, SK-HEP-1 produced glycolic acid, an antioxidant reducing ROS-induced cell death (Diez et al., 2021). Furthermore, among the biomarkers related to ROS responses, only the level of pyroglutamic acid was increased by APAP treatment (hippuric acid and 2 hydroxybutyrate, two important ROS related biomarkers, were not significantly over

expressed in treated conditions). Overall, the signature illustrated disturbance by APAP of the lipids and arginine cell metabolism coupled with only a weak oxidative stress response, triggering a concomitant anti-inflammatory response by the LSECs to APAP (*ie:* glycolysis switch and natural anti-oxidant secretion).

4.4. Identification of the APAP metabolic perturbation in synergy with SK-HEP-1 and HepG2/C3a cocultures

The metabolomic profile of cocultures treated with APAP presented a signature similar to the SK-HEP-1 APAP+. One of the common signatures was the perturbation in nitrogen metabolism, illustrated by the increase in ornithine and glutamic acid secretions. We also observed oxalic acid production, similar to the LSECs APAP+ condition. The GSH and inflammation marker pyroglutamic acid was particularly over expressed in the APAP coculture and similar to the SK-HEP-1 monocultures. In fact, as APAP was “physiologically” loaded into the SK-HEP1 compartment in the coculture and then transferred to the hepatocytes (HepG2/C3a) compartment through the endothelial barrier, it was expected that we find similarities in the signatures of the LSECs APAP+ and coculture APAP+ conditions. The specific metabolomic signature of the coculture consisted of the production of intermediate of TCA cycle (citric, malic, alpha ketoglutaric and fumaric acids). This could reflect either an APAP detoxification process by the liver cells, or an early stage of mitochondrial perturbation either by the NAPQI in HepG2/C3a (Moreno Torres et al., 2022; Chen et al., 2021; Cuykx et al., 2018) or by a stronger toxicity in the LSECs in response to the accumulation of pro-inflammatory cytokines (due to liver cell activity in the presence of APAP) in the medium. The toxicity synergy on LSECs is illustrated by the deterioration in PECAM-1 and stabilin-2 expression. Further investigations are required to follow up this observation, such as cytokine assays and transcriptomic profiling.

The approach presented in this study, based on microfluidic liver cells coculture coupled to metabolomic analysis, succussed to reveal specific biomarker of hepatocytes, LSECs and hepatocytes/LSECs cocultures. In the last years, omics analysis, including metabolomics, have emerged as a promising tool to investigate and elucidate the mechanisms and pathways involved in chemical-induced toxicity and pathologies development (Canzler et al., 2020). The integration of omics approaches with a relevant liver model can provide reliable and effective biomarkers for liver toxicity

and diseases (Canzler et al., 2020, Zeng et al., 2021). Currently, most of the *in vitro* liver models are mainly based on static cultures in Petri dishes and focused on hepatocytes, without considering non-parenchymal cells (NPCs), which play a key role in liver functions, response to xenobiotics and liver diseases, (Bale et al., 2016; Ortega-Ribera et al., 2018; Moradi et al., 2020). Although the present model is based on hepatic cell line, it recapitulates several "physiological-like" situations such as dynamic culture, 3D organization, drug diffusion throughout LSECs barrier and hepatocytes/LSECs interactions. In a proof of concept, the use of HepG2/C3a and SK-HEP-1 cells represent a good compromise between the ease of use/low cost and the expression of certain functions of liver cells. However, further studies, including the use of human primary cells, long-term exposures to drug, dose response curves, and integration of Kupffer (LSECs insert) and stellate (hepatocyte biochip) cells would be needed to improve the relevance of our model. The integration of other omics analysis (transcriptomic and proteomic) would be also interesting to elucidate the mechanisms involved in hepatotoxicity and liver diseases. We are working on those issues and we believe that our approach combining organ-on-chip technology and metabolomic/omics is a step forward in the knowledge of the liver toxicity and pathology.

Conclusions

In summary, we used organ-on-chip technology to investigate liver tissue crosstalk. Our *in vitro* model was based on an apical SK-HEP-1 insert culture coupled with basal 3D HepG2/C3a culture in biochip, simulating the sinusoid by separating LSECs and hepatocytes. We investigated the modifications in the metabolome of SK-HEP-1, HepG2/C3a monocultures, SK-HEP-1/HepG2/C3a cocultures, in a control and in APAP-treated conditions. At the selected concentration, APAP did not present significant hepatoxicity with regard to HepG2/C3a cells. In SK-HEP-1, we detected metabolic switches concomitantly with the apparition of an anti-oxidant marker, but mild levels of ROS biomarkers. The main characteristics of the LSECs APAP+ signature presented significant similarities with those of the SK-HEP-1/HepG2/C3a APAP+ cocultures. These results make it possible to confirm the specificity of each type of cells in the overall APAP coculture signature. They also contribute to show the benefits of such an approach for refining knowledge of liver tissues and cultures when

exposed to drugs. We believe that the combination of a microfluidic coculture, 3D organization and metabolomic profiling could be a promising tool for chemical risk assessment.

Conflicts of interest

HCS pharma is the BIOMIMESYS®Liver owner and is a partner of the ANR MimLiverOnChip (ANR-19-CE19-0020-01). Co-authors Zied Souguir and Nathalie Maubon are employees of HCSPharma.

Acknowledgements

This work and T. Messelmani PhD are funded by ANR (Agence Nationale de la Recherche, France) through the MIMLIVEROnChip project, grant number ANR-19-CE19-0020-01, and by a grant from Contrat de Plan Etat-Région (CPER) Cancer 2015–2020. The authors would like to thank the JSPS Core-to-Core Program (JPJSCCA20190006), the Research Department of the Université de technologie de Compiègne (Research Training Innovation Chair, DOT project - Disruptive Organoids Technologies) and the CNRS (CNRS international research team, TEAMS project – Therapeutics and Engineering Against Metabolic Syndrome, between CNRS/UTC BMBI and CNRS/IIS LIMMS) for their supports. FS is Director of Research at INSERM.

References

Agin, A., Heintz, D., Ruhland, E., Chao de la Barca, J.M., Zumsteg, J., Moal, V., Gauchez, A.S., Namer, I.J., 2016. Metabolomics – an overview. From basic principles to potential biomarkers (part 1). Med. Nucl. 40, 4-10. https://doi.org/10.1016/j.mednuc.2015.12.006.

Badmann, A., Langsch, S., Keogh, A., Brunner, T., Kaufmann, T., Corazza, N., 2012. TRAIL enhances paracetamol-induced liver sinusoidal endothelial cell death in a Bim- and Bid-dependent manner. Cell Death Dis. 3, e447. https://doi.org/10.1038/cddis.2012.185.

Bale, S.S., Geerts, S., Jindal, R., Yarmush, M.L., 2016. Isolation and co-culture of rat parenchymal and non-parenchymal liver cells to evaluate cellular interactions and response. Sci. Rep. 6, 25329. https://doi.org/10.1038/srep25329.

Bhushan, A., Martucci, N.J., Usta, O.B., Yarmush, M.L., 2016. New technologies in drug metabolism and toxicity screening: organ-to-organ interaction. Expert Opin. Drug Metab. Toxicol. 12, 475-477. https://doi.org/10.1517/17425255.2016.1162292.

Bricks, T., Hamon, J., Fleury, M.J., Jellali, R., Merlier, F., Herpe, Y.E., Seyer, A., Regimbeau, J.M., Bois, F.Y., Leclerc, E., 2015. Investigation of omeprazole and phenacetin first-pass metabolism in humans using a microscale bioreactor and pharmacokinetic models. Biopharm. Drugs Dispo. 36, 275-293. https://doi.org/10.1002/bdd.1940.

Bricks, T., Paullier, P., Legendre, A., Fleury, M. J., Zeller, P., Merlier, F., Anton, P. M., & Leclerc, E., 2014. Development of a new microfluidic platform integrating co-cultures of intestinal and liver cell lines. Toxicol. in Vitro 28, 885-895. https://doi.org/10.1016/j.tiv.2014.02.005.

Britt, E.C., Lika, J., Giese, M.A., Schoen, T.J., Seim, G.L., Huang, Z., Lee, P.Y., Huttenlocher, A., Fan, J., 2022. Switching to the cyclic pentose phosphate pathway powers the oxidative burst in activated neutrophils. Nat. Metab. 4, 389-403. https://doi.org/10.1038/s42255-022-00550-8.

Caloni, F., De Angelis, I., Hartung, T., 2022). Replacement of animal testing by integrated approaches to testing and assessment (IATA): a call for in vivitrosi. Arch. Toxicol. 96, 1935-1950. https://doi.org/10.1007/s00204-022-03299-x.

Canzler, S., Schor, J., Busch, W., Schubert, K., Rolle-Kampczyk, U.E., Seitz, H., Kamp, H., von Bergen, M., Buesen, R., Hackermüller, J., 2020. Prospects and challenges of multi-omics data integration in toxicology. Arch. Toxicol. 94, 371-388. https://doi.org/10.1007/s00204-020-02656-y.

Chen, S.S., Huang, Y., Guo, Y.M., Li, S.S., Shi, Z., Niu, M., Zou, Z.S., Xiao, X.H., Wang, J.B., 2021. Serum metabolomic analysis of chronic drug-induced liver injury with or without cirrhosis. Front. Med. 8, 640799. https://doi.org/10.3389/fmed.2021.640799.

Choucha Snouber, L., Bunescu, A., Legallais, C., Brochot, C., Dumas, M.E., Elena-Herrmann, B., Leclerc, E., 2013. Metabolomics-on-a-chip of hepatotoxicity induced by anticancer drug flutamide and its active metabolite hydroxyflutamide using HepG2/C3a microfluidic biochips. Toxicol. Sci. 132, 8-20. https://doi.org/10.1093/toxsci/kfs230.

Cogger, V.C., Mohamad, M., Solon-Biet, S.M., Senior, A.M., Warren, A., O'Reilly, J.N., Tung, B.T., Svistounov, D., McMahon, A.C., Fraser, R., Raubenheimer, D., Holmes, A.J., Simpson, S.J., Le Couteur, D.G., 2016. Dietary macronutrients and the aging lver sinusoidal endothelial cell. Am. J. Physiol. Heart Circ. Physiol. 310, H1064-H1070. https://doi.org/10.1152/ajpheart.00949.2015.

Cuykx, M., Rodrigues, R.M., Laukens, K., Vanhaecke, T., Covaci, A., 2018. *In vitro* assessment of hepatotoxicity by metabolomics: a review. Arch. Toxicol. 92, 3007-3029. https://doi.org/10.1007/s00204-018-2286-9.

Dahlin DC, Miwa GT, Lu AY, Nelson SD. 1984. N-acetyl-p-benzoquinone imine: a cytochrome P-450-mediated oxidation product of acetaminophen. Proc. Natl. Acad. Sci. USA 81, 1327-1331. https://doi.org/10.1073/pnas.81.5.1327.

Dalsbecker, P., Beck Adiels, C., Goksör, M., 2022. Liver-on-a-chip devices: the pros and cons of complexity. Am. J. Physiol. Gastrointest. Liver Physiol. 323, G188-G204. https://doi.org/10.1152/ajpgi.00346.2021.

Diez, V., Traikov, S., Schmeisser, K., Adhikari, A.K.D., Kurzchalia, T.V., 2021, Glycolate combats massive oxidative stress by restoring redox potential in Caenorhabditis elegans. Commun. Biol. 4, 151. https://doi.org/10.1038/s42003-021-01669-2.

Dorovini-Zis, K., Bowman, P.D., Betz, A.L., Goldstein, G.W., 1984. Hyperosmotic arabinose solutions open the tight junctions between brain capillary endothelial cells in tissue culture. Brain Res. 302, 383-386. https://doi.org/10.1016/0006-8993(84)90254-3.

Duarte, I.F., Gil, A.M., 2012. Metabolic signatures of cancer unveiled by NMR spectroscopy of human biofluids. Prog. Nucl. Magn. Reson. Spectrosc. 62, 51-74. https://doi.org/10.1016/j.pnmrs.2011.11.002.

Dudek, M., Lohr, K., Donakonda, S., Baumann, T., Lüdemann, M., Hegenbarth, S., Dübbel, L., Eberhagen, C., Michailidou, S., Yassin, A., Prinz, M., Popper, B., Rose-John, S., Zischka, H., Knolle, P.A., 2022. IL-6-induced FOXO1 activity determines the dynamics of metabolism in CD8 T cells cross-primed by liver sinusoidal endothelial cells. Cell Rep. 38, 110389. https://doi.org/10.1016/j.celrep.2022.110389.

Dufour-Rainfray, D., Lambérioux, M., Boulard, P., Guidotti, M., Delaye, J.B., Ribeiro, M.J., Gauchez, A.S., Balageas, A.C., Emond, P., Agin, A., 2020. Metabolomics – an

overview. from basic principles to potential biomarkers (part 2). Med. Nucl. 44,158-163. https://doi.org/10.1016/j.mednuc.2020.02.004.

Duhault, J., Bure, J., Lonchampt, M.O., Lonchampt, M., Beert, L., Regnault, F., Sicot, N., Boulanger, M., 1979. The effect of high glucose concentration on the proliferation and the synthesis of lipids in endothelial cells in culture. Biomedicine 30, 56-60.

Essaouiba, A., Jellali, R., Gilard, F., Gakière, B., Okitsu, T., Legallais, C., Sakai, Y., & Leclerc, E., 2022. Investigation of the exometabolomic profiles of rat islets of Langerhans cultured in microfluidic biochip. Metabolites 12, 1270. https://doi.org/10.3390/metabo12121270.

Ferry, S., Degli Esposti, M., Ndebele, K., Gona, P., Knight, D., Rosenquist, M., Khosravi-Far, R., 2005. Tumor necrosis factor-related apoptosis-inducing ligand alters mitochondrial membrane lipids. Cancer Res. 65, 8286-8297. https://doi.org/10.1158/0008-5472.CAN-04-1913.

Gall, W.E., Beebe, K., Lawton, K.A., Adam, K.P., Mitchell, M.W., Nakhle, P.J., Ryals, J.A., Milburn, M.V., Nannipieri, M., Camastra, S., Natali, A., Ferrannini, E., RISC Study Group, 2010. alpha-hydroxybutyrate is an early biomarker of insulin resistance and glucose intolerance in a nondiabetic population. PLoS One 5, e10883. https://doi.org/10.1371/journal.pone.0010883.

Geng, Y., 2020. Lipotoxicity in non-alcoholic fatty liver disease: mechanisms and prevention in experimental models. University of Groningen. https://doi.org/10.33612/diss.130260314.

Gromski, P.S., Xu, Y., Hollywood, K.A., Turner, M.L., Goodacre, R., 2015. The influence of scaling metabolomics data on model classification accuracy. Metabolomics 11, 684-695. https://doi.org/10.1007/s11306-014-0738-7.

Guillouzo, A.,1998. Liver cell models in *in vitro* toxicology. Environ. Health Respect. 106, 511-532. https://doi.org/10.1289/ehp.98106511.

Hang, T.C., Lauffenburger, D.A., Griffith, L.G., Stolz, D.B., 2012. Lipids promote survival, proliferation, and maintenance of differentiation of rat liver sinusoidal endothelial cells *in vitro*. Am. J. Physiol. Gastrointest. Liver Physiol. 302, G375-G388. https://doi.org/10.1152/ajpgi.00288.2011.

Iwakiri, Y., Kim, M.Y., 2015. Nitric oxide in liver diseases. Trends Pharmacol. Sci. 36, 524-536. https://doi.org/10.1016/j.tips.2015.05.001.

Jaeschke, H., Duan, L., Nguyen, N., Ramachandran, A., 2019. Mitochondrial damage and biogenesis in acetaminophen-induced liver injury. Liver Res. 3, 150-156. https://doi.org/10.1016/j.livres.2019.10.002.

Jellali, R., Gilard, F., Pandolfi, V., Legendre, A., Fleury, M.J., Paullier, P., Legallais, C., Leclerc, E., 2018. Metabolomics-on-a-chip approach to study hepatotoxicity of DDT, permethrin and their mixtures. J. Appl. Toxicol. 38, 1121-1134. https://doi.org/10.1002/jat.3624.

Jellali, R., Jacques, S., Essaouiba, A., Gilard, F., Letourneur, F., Gakière, B., Legallais, C., & Leclerc, E., 2021. Investigation of steatosis profiles induced by pesticides using liver organ-on-chip model and omics analysis. Food Chem. Toxicol. 152, 112155. https://doi.org/10.1016/j.fct.2021.112155.

Jellali, R., Lereau Bernier, M., Tauran, Y., Gilard, G., Danoy, M., Kido, T., Miyajima, A., Sakai, Y., Leclerc, E., 2020. Metabolomic profiling during the differentiation of human induced pluripotent stem cells into hepatocyte-like cells. Differentiation 112,17-26. https://doi.org/10.1016/j.diff.2019.10.006.

Jellali, R., Paullier, P., Fleury, M.J., Leclerc, E., 2016. Liver and kidney cells cultures in a new perfluoropolyether biochip. Sens. Actuators B Chem. 229, 396-407. https://doi.org/10.1016/j.snb.2016.01.141.

Krähenbühl, L., Reichen, J., Talos, C., Krähenbühl, S., 1997. Benzoic acid metabolism reflects hepatic mitochondrial function in rats with long-term extrahepatic cholestasis. Hepatology 25, 278-283. https://doi.org/10.1053/jhep.1997.v25.pm0009021934.

Leclerc, E., Hamon, J., Claude, I., Jellali, R., Naudot, M., Bois, F., 2015. Investigation of acetaminophen toxicity in HepG2/C3a microscale cultures using a system biology model of glutathione depletion. Cell Biol. Toxicol. 31, 173-185. https://doi.org/10.1007/s10565-015-9302-0.

Li, H., Ding, R., Shan, Y., Ye, F., Lin, Y., Men, X., Chen, C., Tan, S., Wang, Q., Hu, B., 2021. L-arabinose alleviates diabetes-aggravated cerebral ischemic injury by repairing the blood-brain barrier via downregulating NF-κB signals. J. Funct. Foods 87, 104839. https://doi.org/10.1016/j.jff.2021.104839.

Li, M., Wu, Y., Ye, L., 2022. The Role of amino acids in endothelial biology and function. Cells 11, 1372. https://doi.org/10.3390/cells11081372.

Lord, R.S., Bralley, J.A., 2008. Clinical applications of urinary organic acids. Part 1: Detoxification markers. Altern. Med. Rev. 13, 205-215.

Lu, S.C., 1999. Regulation of hepatic glutathione synthesis: current concepts and controversies. FASEB J. 13, 1169-1183.

Messelmani, T., Le Goff, A., Soncin, F., Souguir, Z., Merlier, F., Maubon, N., Legallais, C., Leclerc, E., Jellali, R., 2023. Coculture model of a liver sinusoidal endothelial cell barrier and hepatocyte spheroids-on-chip in an advanced fluidic platform. Authorea. DOI: 10.22541/au.167596570.02002054/v1.

Messelmani, T., Morisseau, L., Sakai, Y., Legallais, C., Le Goff, A., Leclerc, E., Jellali, R., 2022a. Liver organ-on-chip models for toxicity studies and risk assessment. Lab chip 22, 2423-2450. https://doi.org/10.1039/d2lc00307d.

Messelmani, T., Le Goff, A., Souguir, Z., Maes, V., Roudaut, M., Vandenhaute, E., Maubon, N., Legallais, C., Leclerc, E., Jellali, R., 2022b. Development of liver-on-chip integrating a hydroscaffold mimicking the liver's extracellular matrix. Bioengineering 9, 443. https://doi.org/10.3390/bioengineering9090443.

Milam, K.M., Byard, J.L., 1985. Acetaminophen metabolism, cytotoxicity, and genotoxicity in rat primary hepatocyte cultures. Toxicol. Appl. Pharmacol. 79, 342-347. https://doi.org/10.1016/0041-008x(85)90356-4.

Moradi, E., Jalili-Firoozinezhad, S., Solati-Hashjin, M., 2020. Microfluidic organ-on-a-chip models of human liver tissue. Acta Biomater. 116, 67-83. https://doi.org/10.1016/j.actbio.2020.08.041.

Moreno-Torres, M., Quintás, G., Castell, J.V., 2022. The potential role of metabolomics in drug-induced liver injury (DILI) assessment. Metabolites 12, 564. https://doi.org/10.3390/metabo12060564.

Mueller, D., Krämer, L., Hoffmann, E., Klein, S., Noor, F., 2014. 3D organotypic HepaRG cultures as *in vitro* model for acute and repeated dose toxicity studies. Toxicol. in vitro 28, 104-112. https://doi.org/10.1016/j.tiv.2013.06.024.

Ortega-Ribera, M., Fernández-Iglesias, A., Illa, X., Moya, A., Molina, V., Maeso-Díaz, R., Fondevila, C., Peralta, C., Bosch, J., Villa, R., Gracia-Sancho, J., 2018. Resemblance of the human liver sinusoid in a fluidic device with biomedical and pharmaceutical applications. Biotechnol. Bioeng. 2585-2594. https://doi.org/10.1002/bit.26776.

Ouattara, D.A., Prot, J.M., Bunescu, A., Dumas, M.E., Elena-Herrmann, B., Leclerc, E., Brochot, C., 2012. Metabolomics-on-a-chip and metabolic flux analysis for label-free modeling of the internal metabolism of HepG2/C3A cells. Mol. Biosyst. 8, 1908-1920. https://doi.org/10.1039/c2mb25049g.

Oyama, T., Miyasita, Y., Watanabe, H., Shirai, K., 2006. The role of polyol pathway in high glucose-induced endothelial cell damages. Diabetes Res. Clin. Pract. 73, 227-234. https://doi.org/10.1016/j.diabres.2006.02.010

Pang, Z., Chong, J., Zhou, G., de Lima Morais, D.A., Chang, L., Barrette, M., Gauthier, C., Jacques, P.E., Li, S., Xia, J., 2021. Metabo-Analyst 5.0: narrowing the gap between raw spectra and functional insights. Nucleic Acids Res. 49, W388-W396. https://doi.org/10.1093/nar/gkab382.

Pi, X., Xie, L., Patterson, C., 2018. Emerging roles of vascular endothelium in metabolic homeostasis. Circ. Res. 123, 477-494. https://doi.org/10.1161/CIRCRESAHA.118.313237.

Prot, J.M., Bunescu, A., Elena-Herrmann, B., Aninat, C., Snouber, L.C., Griscom, L., Razan, F., Bois, F.Y., Legallais, C., Brochot, C., Corlu, A., Dumas, M.E., Leclerc, E., 2012. Predictive toxicology using systemic biology and liver microfluidic "on chip" approaches: application to acetaminophen injury. Toxicol. Appl. Pharmacol. 259, 270-280. https://doi.org/10.1016/j.taap.2011.12.017.

Reid, A.B., Kurten, R.C., McCullough, S.S., Brock, R.W., Hinson, J.A., 2005. Mechanisms of acetaminophen-induced hepatotoxicity: role of oxidative stress and mitochondrial permeability transition in freshly isolated mouse hepatocytes. J. Pharmacol. Exp. Ther. 312, 509-516. https://doi.org/10.1124/jpet.104.075945.

Rim, K.T., 2020). In silico prediction of toxicity and its applications for chemicals at work. Toxicol. Environ. Health Sci. 12, 191-202. https://doi.org/10.1007/s13530-020-00056-4.

Ruoß, M., Vosough, M., Königsrainer, A., Nadalin, S., Wagner, S., Sajadian, S., Huber, D., Heydari, Z., Ehnert, S., Hengstler, J.G., Nussler, A.K., 2020. Towards improved hepatocyte cultures: Progress and limitations. Food Chem. Toxicol. 138, 111188. https://doi.org/10.1016/j.fct.2020.111188.

Schnackenberg, L.K., Sun, J., Bhattacharyya, S., Gill, P., James, L.P., Beger, R.D., 2017. Metabolomics analysis of urine samples from children after acetaminophen overdose. Metabolites 7, 46. https://doi.org/10.3390/metabo7030046.

Shah, A.D., Wood, D.M., Dargan, P.I., 2011. Understanding lactic acidosis in paracetamol (acetaminophen) poisoning. Br. J. Clin. Pharmacol. 71, 20-28. https://doi.org/10.1111/j.1365-2125.2010.03765.x.

Shen, C., Zhang, G., Qiu, H., Meng, Q., 2006. Acetaminophen-induced hepatotoxicity of gel entrapped rat hepatocytes in hollow fibers. Chem. Bio.l Interact. 162, 53-61. https://doi.org/10.1016/j.cbi.2006.05.005.

Shintu, L., Baudoin, R., Navratil, V., Prot, J.M., Pontoizeau, C., Defernez, M., Blaise, B., Domange, C., Péry, A., Toulhoat, P., Legallais, C., Brochot, C., Leclerc, E., Dumas, M.E., 2012. Metabolomics-on-a-chip and predictive systems toxicology in microfluidic bioartificial organs. Anal. Chem. 84, 1840-1848. https://doi.org/10.1021/ac2011075.

Song, Q., Chen, H., Li, Y., Zhou, H., Han, Q., & Diao, X., 2016. Toxicological effects of benzo(a)pyrene, DDT and their mixture on the green mussel Perna viridis revealed by proteomic and metabolomic approaches. Chemosphere, 144, 214-224. https://doi.org/10.1016/j.chemosphere.2015.08.029.

Stanimirovic, J., Obradovic, M., Zafirovic, S., Resanovic, I., Bogdanovic, N., Gluvic, Z., Mousa, S.A., Isenovic, E.R., 2015. Effects of altered hepatic lipid metabolism on regulation of hepatic iNOS. Clin. Lipidol. 10, 167-175. https://doi.org/10.2217/clp.15.8.

Tsaioun, K., Blaauboer, B.J., Hartung, T., 2016. Evidence-based absorption, distribution, metabolism, excretion (ADME) and its interplay with alternative toxicity methods. ALTEX 33, 343-358. https://doi.org/10.14573/altex.1610101.

Wang, X.K., Peng, Z.G., 2021. Targeting liver sinusoidal endothelial cells: An attractive therapeutic strategy to control inflammation in nonalcoholic fatty liver disease. Front. Pharmacol. 12, 655557. https://doi.org/10.3389/fphar.2021.655557.

Wong, B.W., Marsch, E., Treps, L., Baes, M., Carmeliet, P., 2017. Endothelial cell metabolism in health and disease: impact of hypoxia. EMBO J. 36, 2187-2203. https://doi.org/10.15252/embj.201696150.

Xie, G., Wang, X., Wang, L., Wang, L., Atkinson, R.D., Kanel, G.C., Gaarde, W.A., Deleve, L.D., 2012. Role of differentiation of liver sinusoidal endothelial cells in progression and regression of hepatic fibrosis in rats. Gastroenterology 142, 918-927.e6. https://doi.org/10.1053/j.gastro.2011.12.017.

Yagasaki, K., Morisaki-Tsuji, N., Miura, A., Funabiki, R., 2002. Possible involvement of phospholipase C and protein kinase C in stimulatory actions of L-leucine and its keto acid, alpha-ketoisocaproic acid, on protein synthesis in RLC-16 hepatocytes. Cytotechnology 40, 151-154. https://doi.org/10.1023/A:1023988405518.

Yang, X., Salminen, W., Schackenberg, L., 2012. Current and emerging biomarkers of hepatotoxicity. Curr. Biomark. Find. 2, 43-55. https://doi.org/10.2147/CBF.S27901.

Zeller, P., Legendre, A., Jacques, S., Fleury, M.J., Gilard, F., Tcherkez, G., Leclerc, E., 2017. Hepatocyte-Sertoli cells coculture in bioreactor improves the Sertoli barrier permeability. J. Appl. Toxicol. 37, 287-295. https://doi.org/10.1002/jat.3360.

Zeng, Y., Wang, X., He, H., Yang, L., Li, S., An, Z., 2021; Integrating multi-Omics reveals crucial biomarkers in non-alcoholic fatty liver disease. SSRN. http://dx.doi.org/10.2139/ssrn.3915431.

Table 1: Albumin and urea secretion, and paracetamol concentration in the basal compartment of different cultures ($^{\#, *, \neq}$ data statistically different, $P < 0,05$).

	Albumin (ng/h)	Urea (µg/h)	Basal APAP (µM) [a]
SK-HEP-1	/	/	/
HepG2/C3a	114.2 ± 16.6	$2.14 \pm 0.44^{*\neq}$	/
SK-HEP-1/HepG2/C3A coculture	129.7 ± 27.6	$1.19 \pm 0.16^{*\#}$	/
SK-HEP-1 APAP+	---	/	103 ± 7
HepG2/C3a APAP+	113.4 ± 5.9	$0.51 \pm 0.18^{\neq}$	84 ± 5
SK-HEP-1/HepG2/C3A coculture APAP+	127.6 ± 21.7	$0.65 \pm 0.23^{\#}$	87 ± 8

[a] Data from Messelmani et al., 2013.

Fig.1. (A) Design and principle of the IIDMP device; (B) experimental procedure for cell cultures.

Fig.2. Characterisation of the SK-HEP-1 endothelial barrier in dynamic monoculture and coculture (with and without APAP, 8 days of maturation followed by 2 days in the IIDMP platform). (A) cell morphologies; (B) actin, nuclei, PECAM-1 and stabilin-2 staining of SK-HEP-1 monoculture and coculture without APAP; (C) actin, nuclei, PECAM-1 and stabilin-2 staining of SK-HEP-1 monoculture and coculture exposed to APAP.

Fig.3. Characterisation of HepG2/C3a cells cultured in the biochip, in monoculture and coculture (with and without APAP). (A) cell morphology after seeding and after 24 h of adhesion in static conditions; (B) cell morphology after 48 h of dynamic culture; (C) and (D) actin and nuclei (DAPI) staining after 48 h of dynamic coculture.

Fig.4. Global multivariate statistical analysis of SK-HEP-1 monoculture, HepG2/C3a monoculture, SK-HEP-1/HepG2/C3a coculture and basal medium metabolomic profiles. (A) PLS-DA scores plot discriminating different culture modes; (B) heatmap of the top 40 metabolites significantly modulated ($P < 0.05$ and VIP > 1; * glycerol 1-phosphate, ** 2-ketoisocaproic acid, # 3-methyl-2-oxobutanoic acid, ≠ 2,3-dihydroxypyridine, ¤ glucose-6-phosphate). Each dot in PLS-DA score plots corresponds to one replicate (n = 5 replicates from three independent experiments).

Fig.5. Comparison of metabolomic profiles of HepG2/C3a cultured in biochip, with and without APAP treatment. (A) OPLS-DA score plot of biochip control culture compared to biochip treated with APAP ($R^2 = 0.73$, $Q^2 = 0.47$); (B) volcano plot (log2 fold change (treated biochip/control biochip) plotted against –log10 P-value) highlighting metabolites differentially expressed between HepG2/C3a control and HepG2/C3a treated with APAP (metabolites upregulated and downregulated in the treated cultures are labelled in red and blue, respectively); (C) heatmap of the 13 metabolites significantly modulated ($P < 0.05$, VIP > 1, * glycerol 1-phosphate, ** glucose-6-phosphate); (D) pathway impact enrichment based on metabolites discriminating HepG2/C3a control and HepG2/C3a treated with APAP. Each dot

in OPLS-DA score plots and column in heatmap correspond to one replicate (n = 5 replicates from three independent experiments).

Fig.6. Comparison of metabolomic profiles of SK-HEP-1 barrier culture, with and without APAP treatment. (A) OPLS-DA score plot of SK-HEP-1 control culture compared to SK-HEP-1 treated with APAP (R^2 = 0.84, Q^2 = 0.74); (B) volcano plot (log2 fold change (treated culture/control culture) plotted against –log10 P-value) highlighting metabolites significantly modulated between SK-HEP-1 control and SK-HEP-1 treated with APAP (metabolites upregulated and downregulated in the treated cultures are labelled in red and blue, respectively); (C) heatmap of the 26 metabolites discriminating both cultures (P < 0;05 and VIP > 1, * trans-4-hydroxy-L-proline, ** glycerol 1-phosphate) (D) Pathway impact enrichment extracted from comparison of SK-HEP-1 culture with and without APAP. Each dot in OPLS-DA score plots and column in heatmap correspond to one replicate (n = 5 replicates from three independent experiments).

Fig.7. Comparison of metabolomes of HepG2/C3a/SK-HEP-1 coculture, with and without APAP treatment. (A) OPLS-DA score plot discriminating both culture conditions (R^2 = 0.82, Q^2 = 0.77); (B) volcano plot (log2 fold change (APAP/control) plotted against –log10 P-value) discriminating metabolites differentially expressed between coculture control and coculture exposed to APAP (metabolites upregulated and downregulated in the treated cocultures are labelled in red and blue, respectively); (C) heatmap of the 27 metabolites significantly modulated (P < 0.05 and VIP > 1, * glycerol 1-phosphate, ** 3-methyl-2-oxobutanoic acid, # 2-ketoisocaproic acid, ≠ alpha ketoglutaric acid); (D) pathway impact enrichment based on 27 metabolites modulated between coculture with and without APAP. Each dot in OPLS-DA score plots and column in heatmap correspond to one replicate (n = 5 replicates from three independent experiments).

Fig.8. Venn diagram showing the specific and common signature between the different culture conditions.

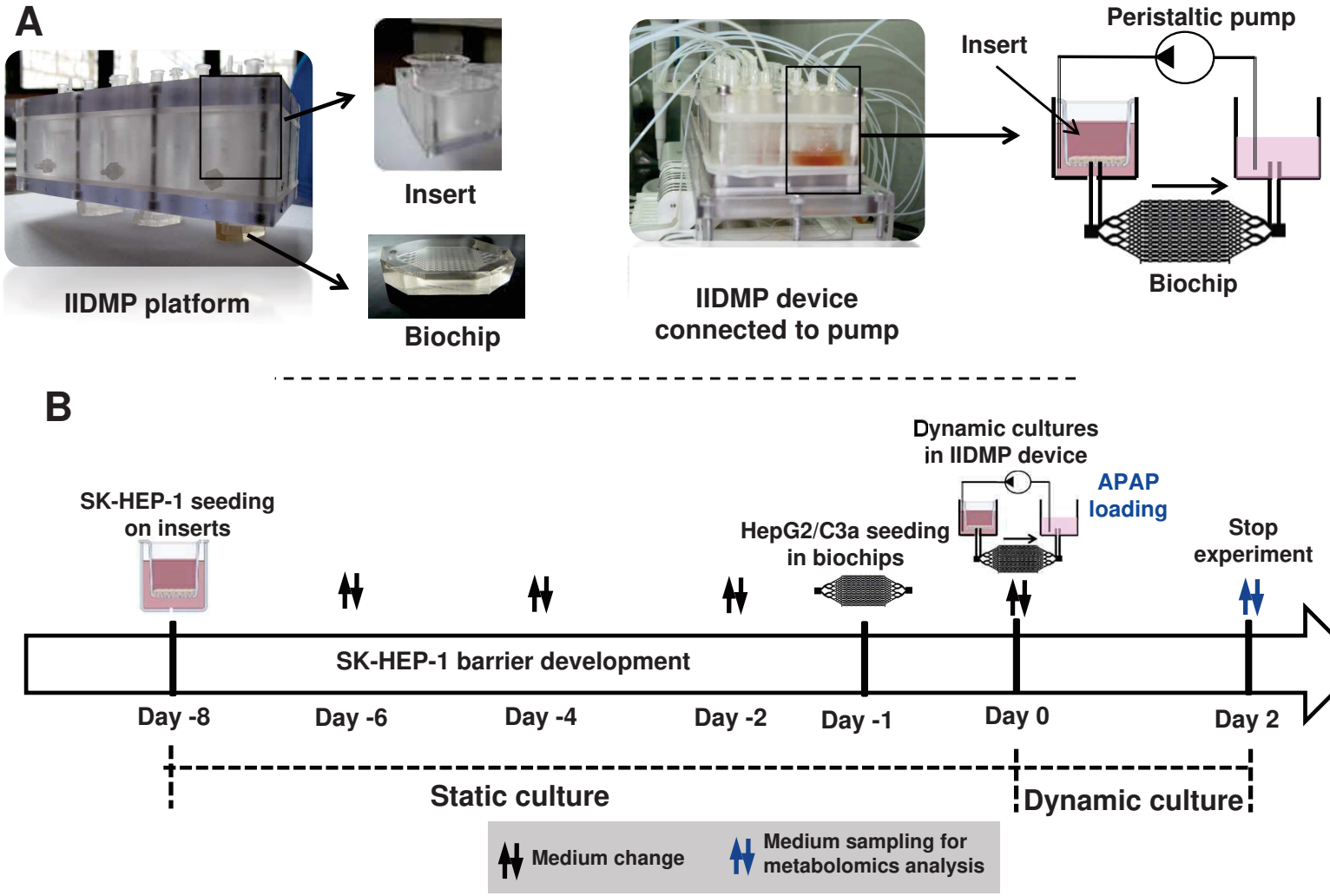
A
IIDMP platform
Insert
Biochip
IIDMP device
connected to pump
Insert
Peristaltic pump
Biochip
B
SK-HEP-1 seeding
on inserts
HepG2/C3a seeding
in biochips
Dynamic cultures
in IIDMP device
APAP
loading
Stop
experiment
SK-HEP-1 barrier development
Day -8
Day -6
Day -4
Day -2
Day -1
Day 0
Day 2
Static culture
Dynamic culture
Medium change
Medium sampling for
metabolomics analysis

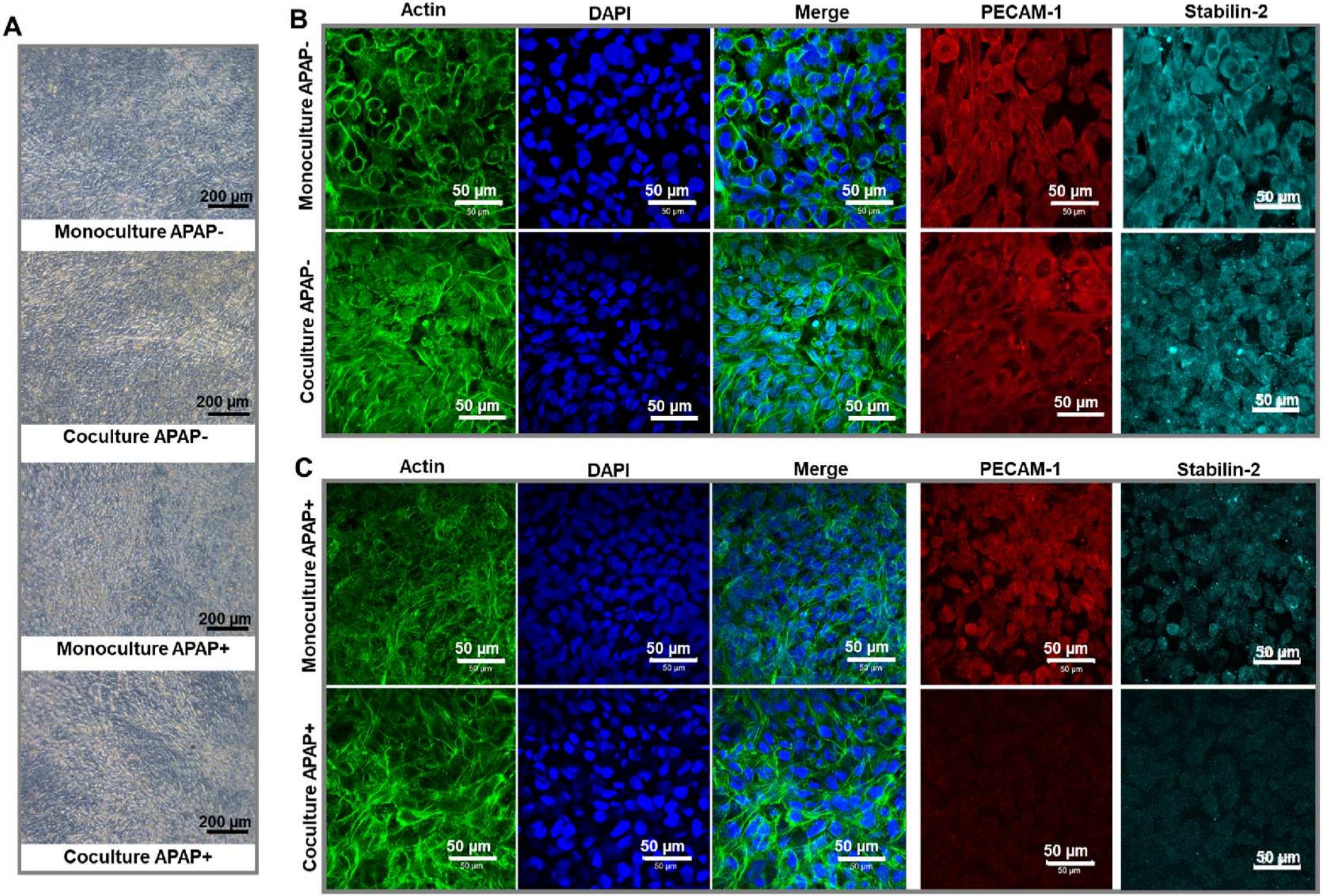
A
200 µm
Monoculture APAP-
200 µm
Coculture APAP-
200 µm
Monoculture APAP+
200 µm
Coculture APAP+
B
Actin
DAPI
Merge
PECAM-1
Stabilin-2
Monoculture APAP-
Coculture APAP-
50 µm
C
Actin
DAPI
Merge
PECAM-1
Stabilin-2
Monoculture APAP+
Coculture APAP+
50 µm

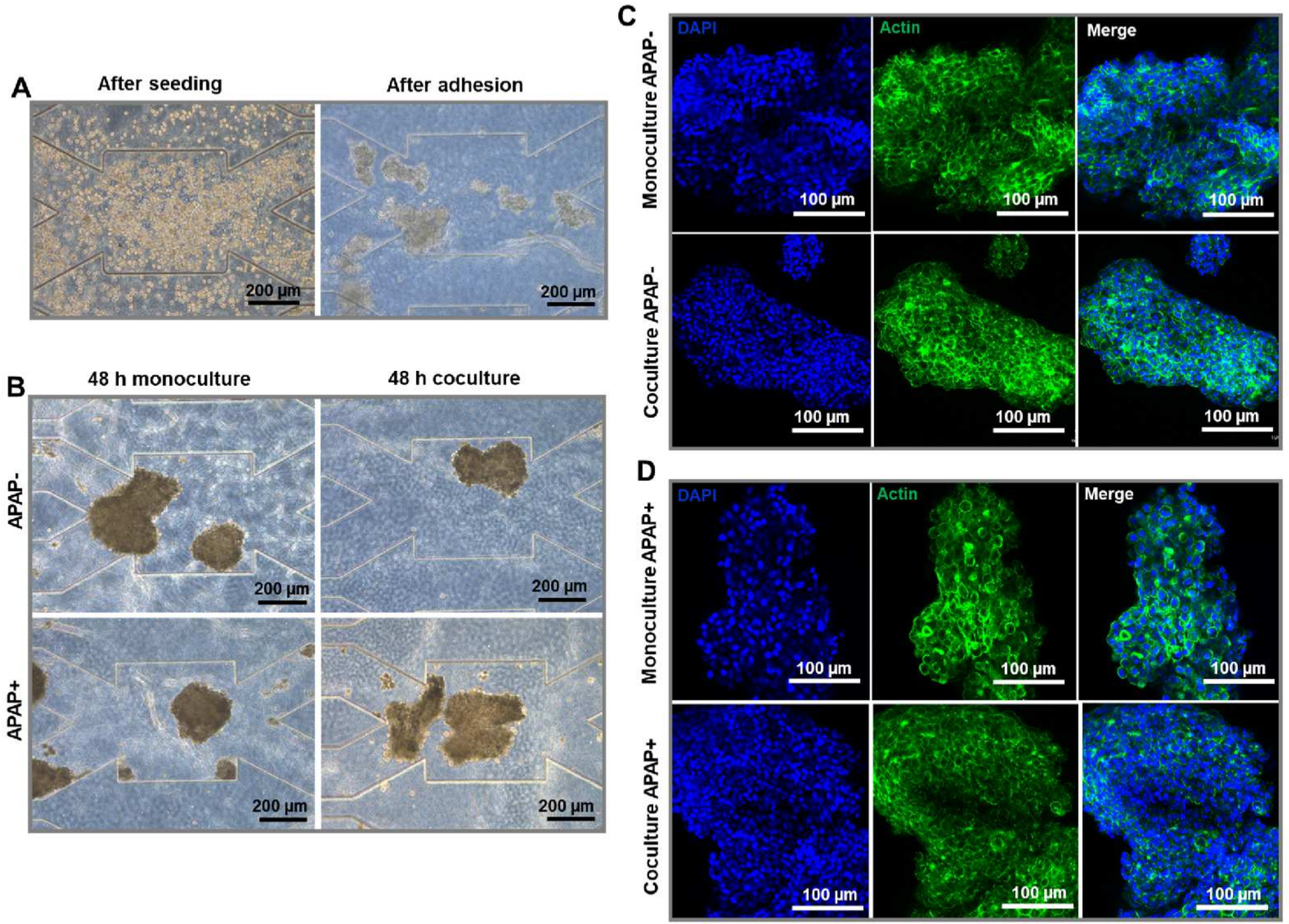
A
After seeding
After adhesion
200 µm
200 µm
B
48 h monoculture
48 h coculture
APAP-
APAP+
200 µm
200 µm
200 µm
200 µm
C
Monoculture APAP-
Coculture APAP-
DAPI
Actin
Merge
100 µm
100 µm
100 µm
100 µm
100 µm
100 µm
D
Monoculture APAP+
Coculture APAP+
DAPI
Actin
Merge
100 µm
100 µm
100 µm
100 µm
100 µm
100 µm

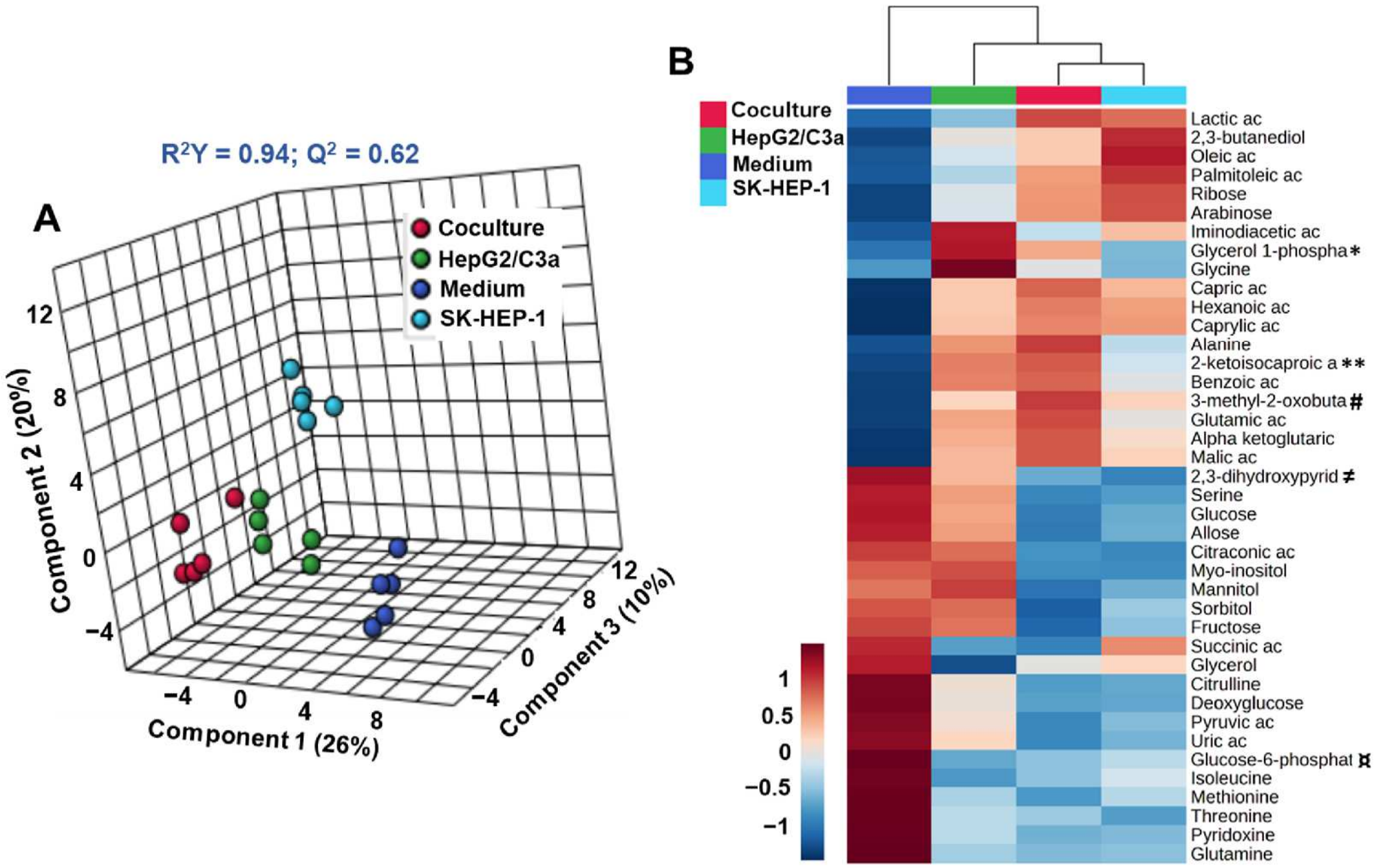
A
R²Y = 0.94; Q² = 0.62
Coculture
HepG2/C3a
Medium
SK-HEP-1
Component 2 (20%)
Component 1 (26%)
Component 3 (10%)
B
Coculture
HepG2/C3a
Medium
SK-HEP-1
Lactic ac
2,3-butanediol
Oleic ac
Palmitoleic ac
Ribose
Arabinose
Iminodiacetic ac
Glycerol 1-phospha*
Glycine
Capric ac
Hexanoic ac
Caprylic ac
Alanine
2-ketoisocaproic a**
Benzoic ac
3-methyl-2-oxobuta#
Glutamic ac
Alpha ketoglutaric
Malic ac
2,3-dihydroxypyrid≠
Serine
Glucose
Allose
Citraconic ac
Myo-inositol
Mannitol
Sorbitol
Fructose
Succinic ac
Glycerol
Citrulline
Deoxyglucose
Pyruvic ac
Uric ac
Glucose-6-phosphat¤
Isoleucine
Methionine
Threonine
Pyridoxine
Glutamine

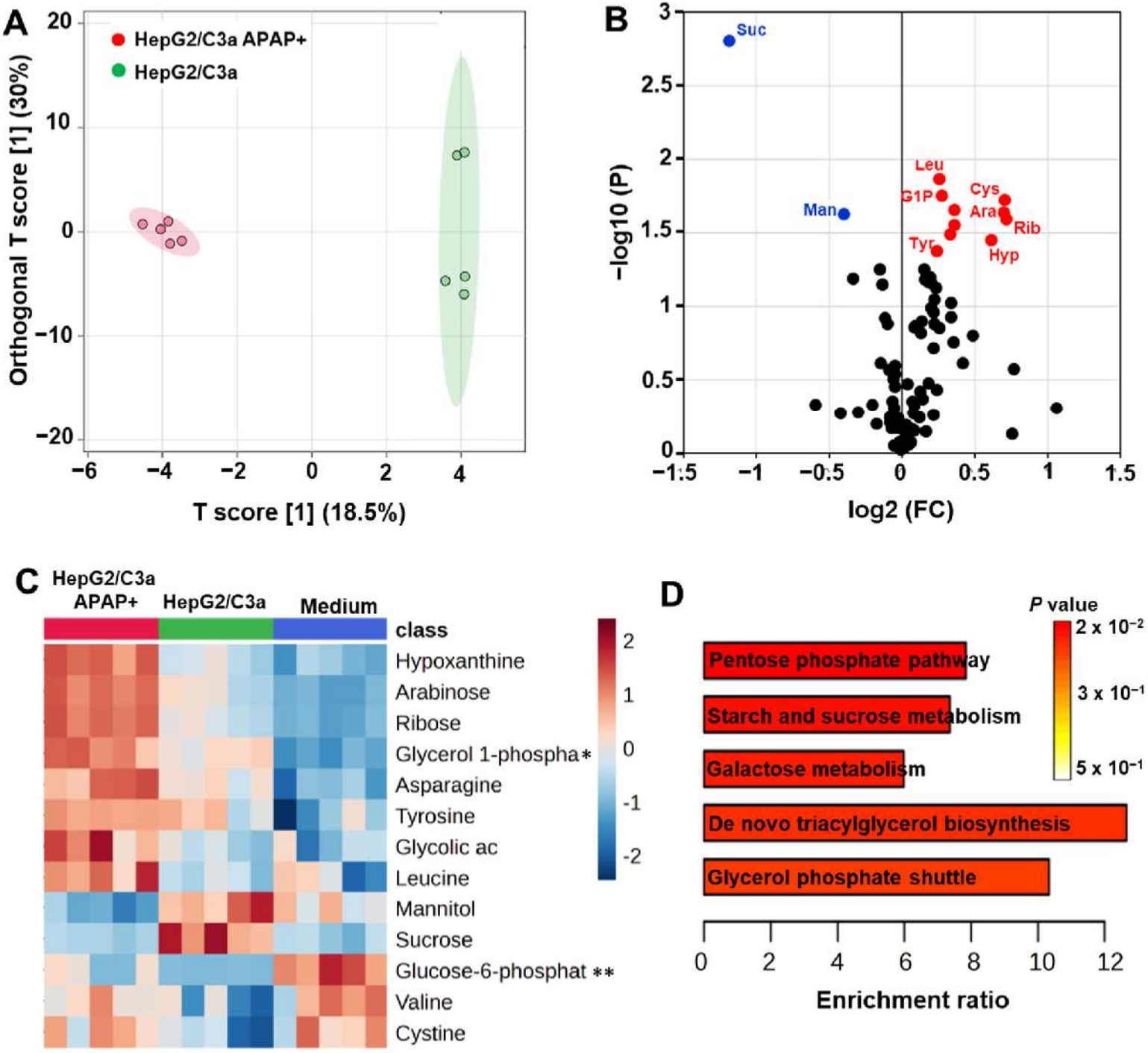
A
HepG2/C3a APAP+
HepG2/C3a
Orthogonal T score [1] (30%)
T score [1] (18.5%)
B
Suc
Man
Leu
G1P
Cys
Ara
Rib
Tyr
Hyp
−log10 (P)
log2 (FC)
C
HepG2/C3a APAP+
HepG2/C3a
Medium
class
Hypoxanthine
Arabinose
Ribose
Glycerol 1-phospha*
Asparagine
Tyrosine
Glycolic ac
Leucine
Mannitol
Sucrose
Glucose-6-phosphat **
Valine
Cystine
D
P value
2 x 10−2
3 x 10−1
5 x 10−1
Pentose phosphate pathway
Starch and sucrose metabolism
Galactose metabolism
De novo triacylglycerol biosynthesis
Glycerol phosphate shuttle
Enrichment ratio

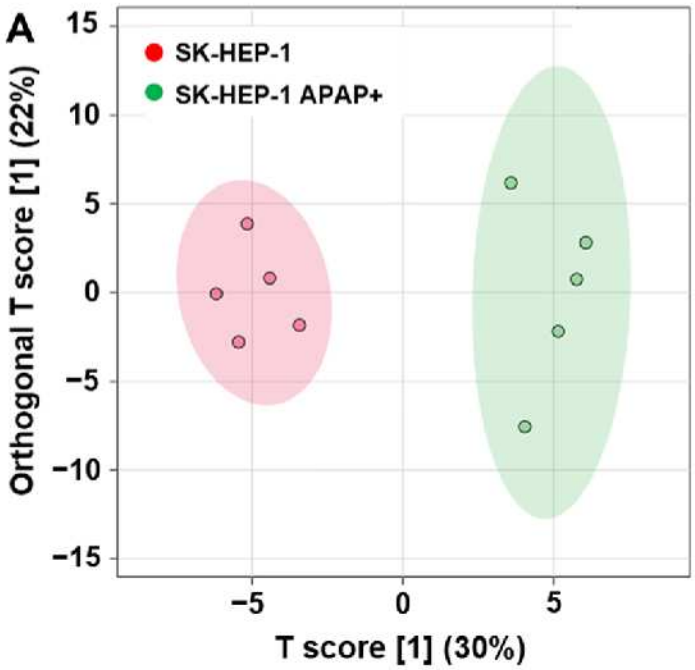
A
SK-HEP-1
SK-HEP-1 APAP+
Orthogonal T score [1] (22%)
T score [1] (30%)

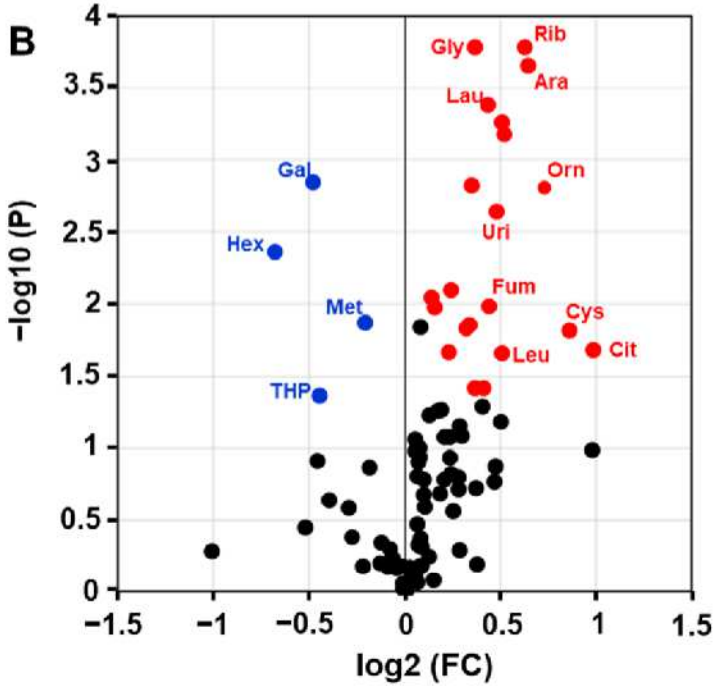
B
Gly
Rib
Ara
Lau
Gal
Orn
Uri
Hex
Fum
Met
Cys
Leu
Cit
THP
−log10 (P)
log2 (FC)

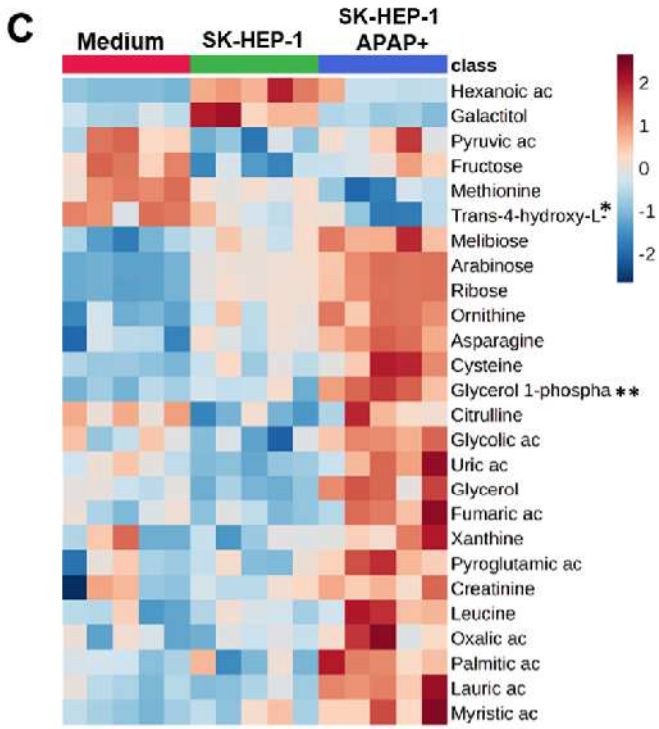
C
Medium
SK-HEP-1
SK-HEP-1 APAP+
class
Hexanoic ac
Galactitol
Pyruvic ac
Fructose
Methionine
Trans-4-hydroxy-L-*
Melibiose
Arabinose
Ribose
Ornithine
Asparagine
Cysteine
Glycerol 1-phospha**
Citrulline
Glycolic ac
Uric ac
Glycerol
Fumaric ac
Xanthine
Pyroglutamic ac
Creatinine
Leucine
Oxalic ac
Palmitic ac
Lauric ac
Myristic ac

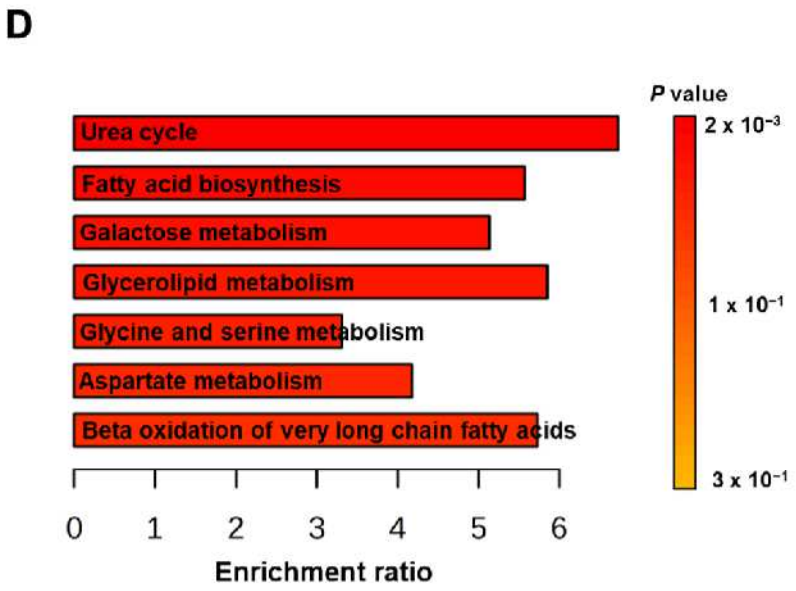
D
Urea cycle
Fatty acid biosynthesis
Galactose metabolism
Glycerolipid metabolism
Glycine and serine metabolism
Aspartate metabolism
Beta oxidation of very long chain fatty acids
Enrichment ratio
P value

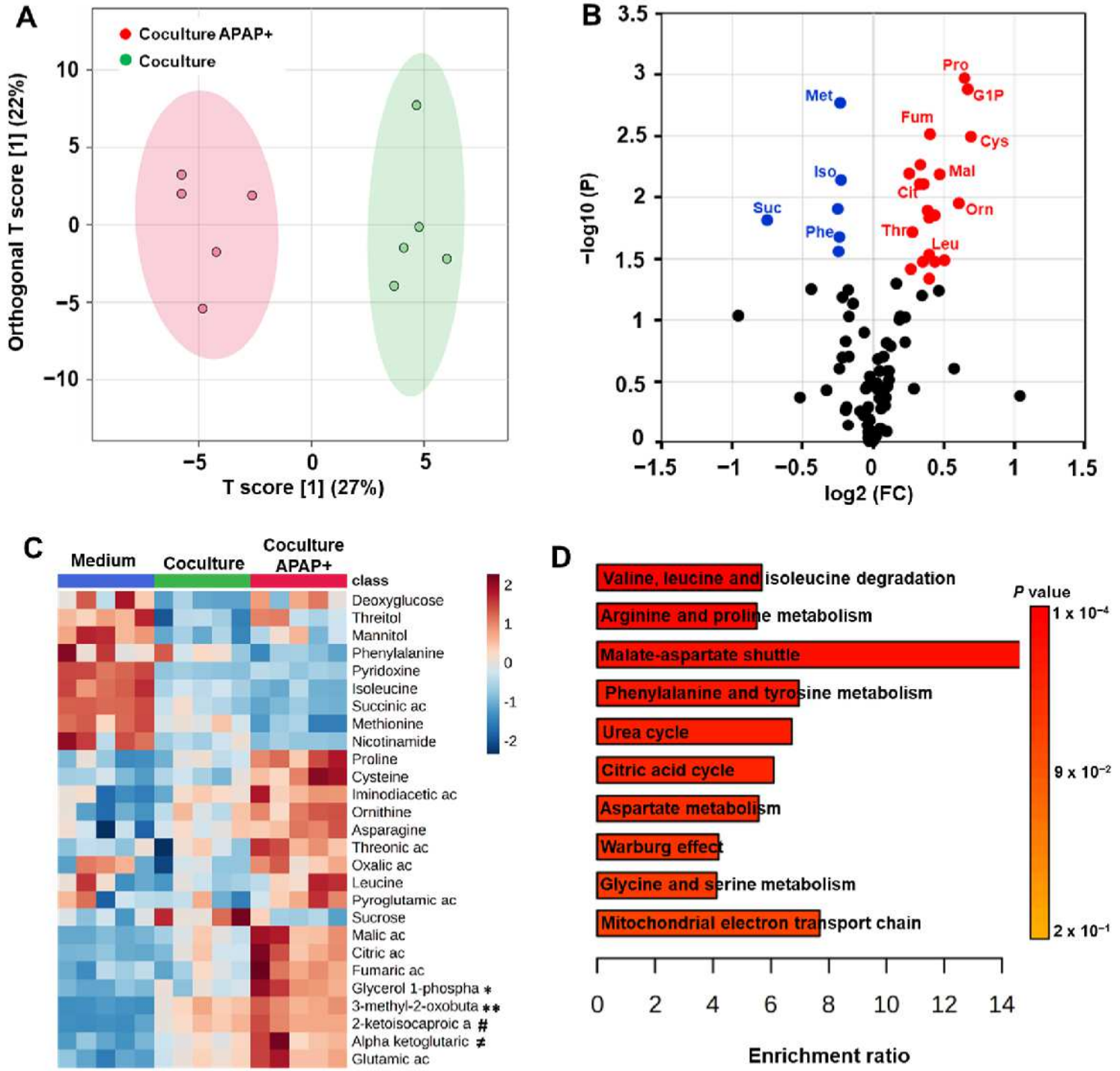
A
Coculture APAP+
Coculture
Orthogonal T score [1] (22%)
T score [1] (27%)
B
−log10 (P)
log2 (FC)
Pro
G1P
Met
Fum
Cys
Iso
Mal
Cit
Suc
Orn
Phe
Thr
Leu
C
Medium
Coculture
Coculture APAP+
class
Deoxyglucose
Threitol
Mannitol
Phenylalanine
Pyridoxine
Isoleucine
Succinic ac
Methionine
Nicotinamide
Proline
Cysteine
Iminodiacetic ac
Ornithine
Asparagine
Threonic ac
Oxalic ac
Leucine
Pyroglutamic ac
Sucrose
Malic ac
Citric ac
Fumaric ac
Glycerol 1-phospha *
3-methyl-2-oxobuta **
2-ketoisocaproic a #
Alpha ketoglutaric ≠
Glutamic ac
D
Valine, leucine and isoleucine degradation
Arginine and proline metabolism
Malate-aspartate shuttle
Phenylalanine and tyrosine metabolism
Urea cycle
Citric acid cycle
Aspartate metabolism
Warburg effect
Glycine and serine metabolism
Mitochondrial electron transport chain
P value
Enrichment ratio

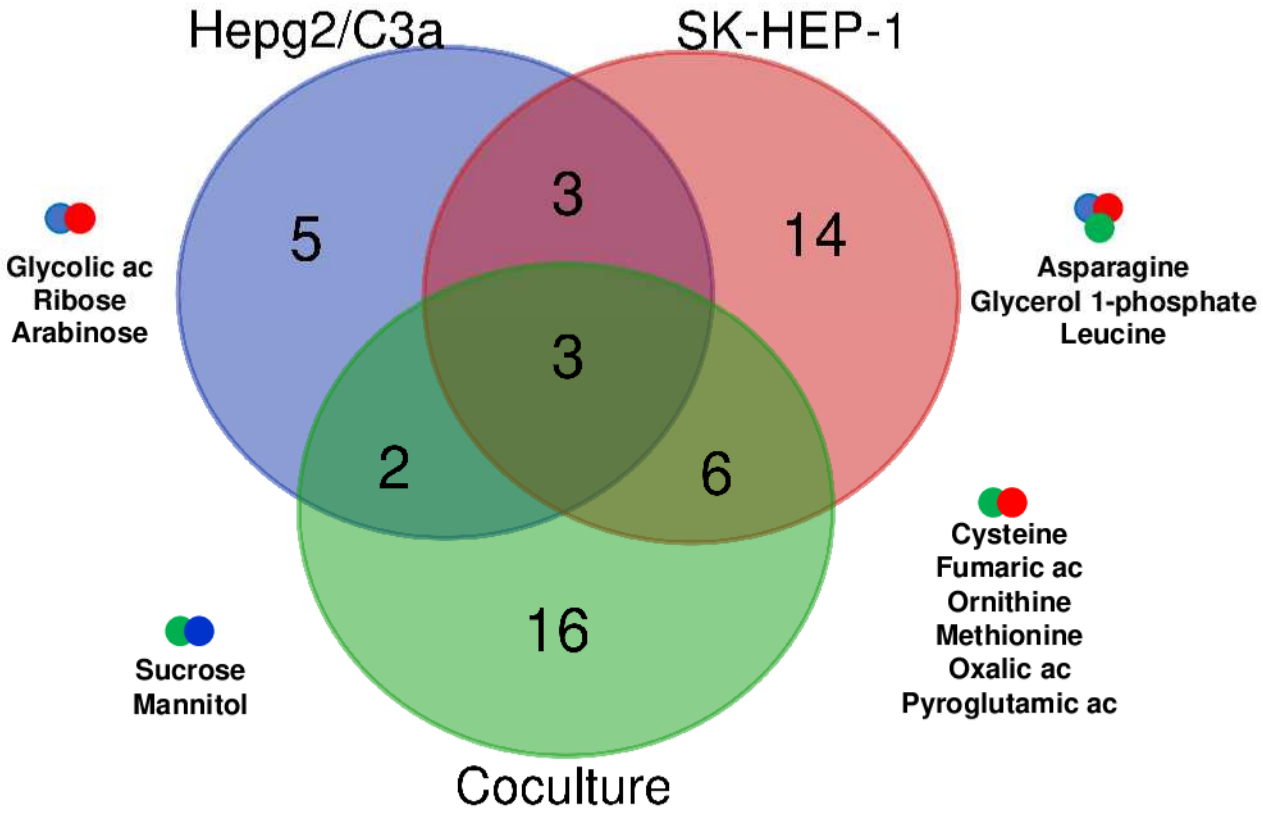
Hepg2/C3a
SK-HEP-1
Coculture
5
3
14
3
2
6
16
Glycolic ac
Ribose
Arabinose
Asparagine
Glycerol 1-phosphate
Leucine
Cysteine
Fumaric ac
Ornithine
Methionine
Oxalic ac
Pyroglutamic ac
Sucrose
Mannitol

Investigation of the metabolomic crosstalks between liver sinusoidal endothelial cells and hepatocytes exposed to paracetamol using organ-on-chip technology

Taha Messelmani [1], Anne Le Goff [1], Fabrice Soncin [2,3], Françoise Gilard [4], Zied Souguir [5], Nathalie Maubon [5], Bertrand Gakière [4], Cécile Legallais [1], Eric Leclerc [1,3], Rachid Jellali [1]*

Supplementary figures/tables

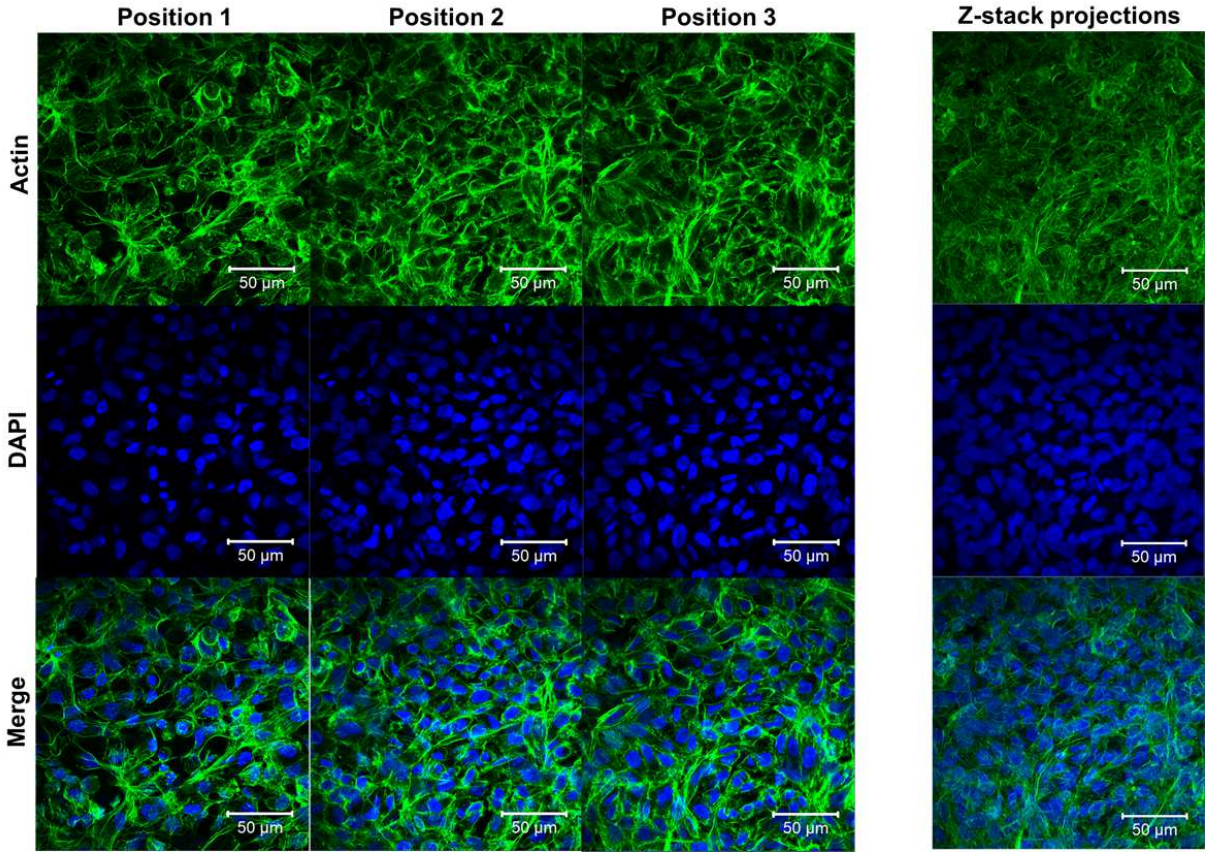

Fig.S1. F-actin (green) and nuclei (blue) stainings of SK-HEP-1 monocultures after 10 days of culture (8 days of maturation in static inserts and 2 days of dynamic culture in IIDMP platform). The images correspond to different Z positions and the z-stack projections.

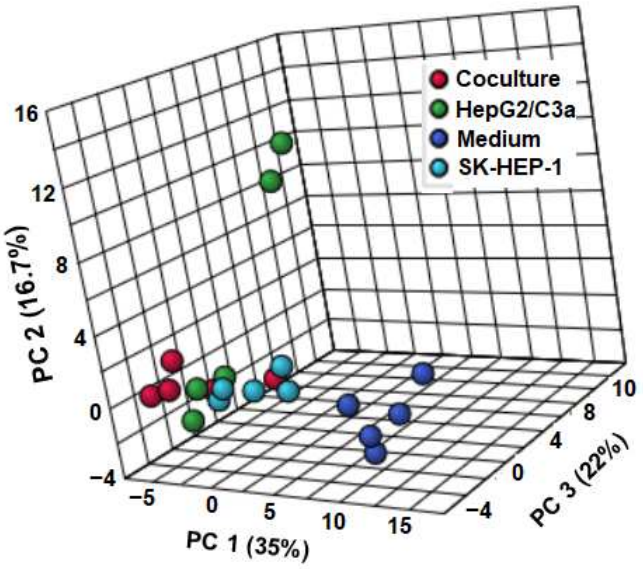

Fig.S2. PCA score plot extracted from the multivariate statistical analysis of SK-HEP-1 monoculture, HepG2/C3a monoculture, SK-HEP-1/HepG2/C3a coculture and basal medium metabolomic profiles. Each dot corresponds to one replicate, n = 5 replicates from three independent experiments.

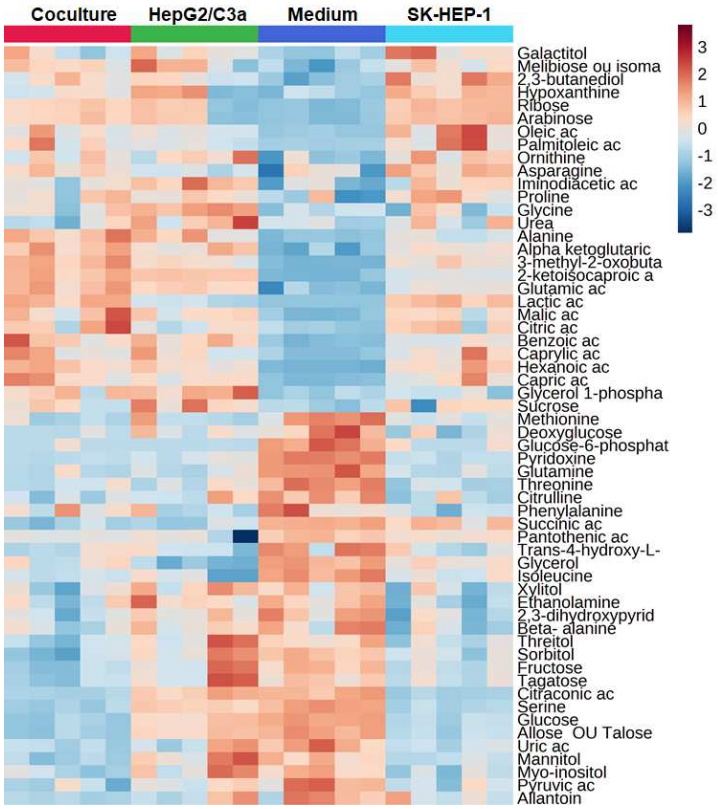

Fig.S3. Heatmap of the 58 metabolites differentially expressed between SK-HEP-1 monoculture, HepG2/C3a monoculture, SK-HEP-1/HepG2/C3a coculture and basal culture medium ($P < 0.05$ and VIP > 1).

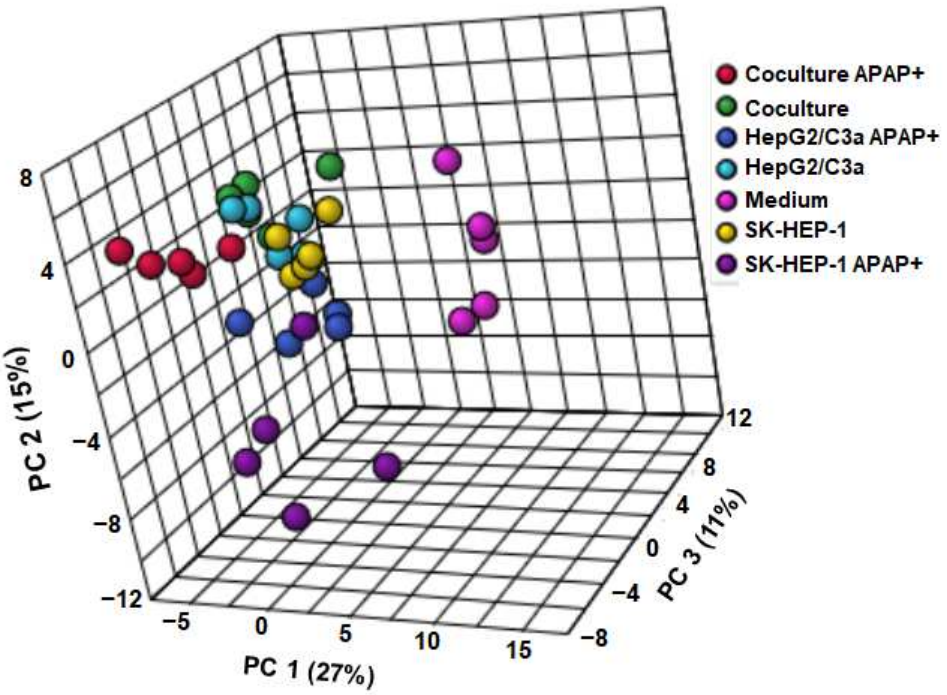

Fig.S4. PCA score plot extracted from the multivariate statistical analysis of metabolomic profiles of all samples. Each dot corresponds to one replicate, n = 5 replicates from three independent experiments.

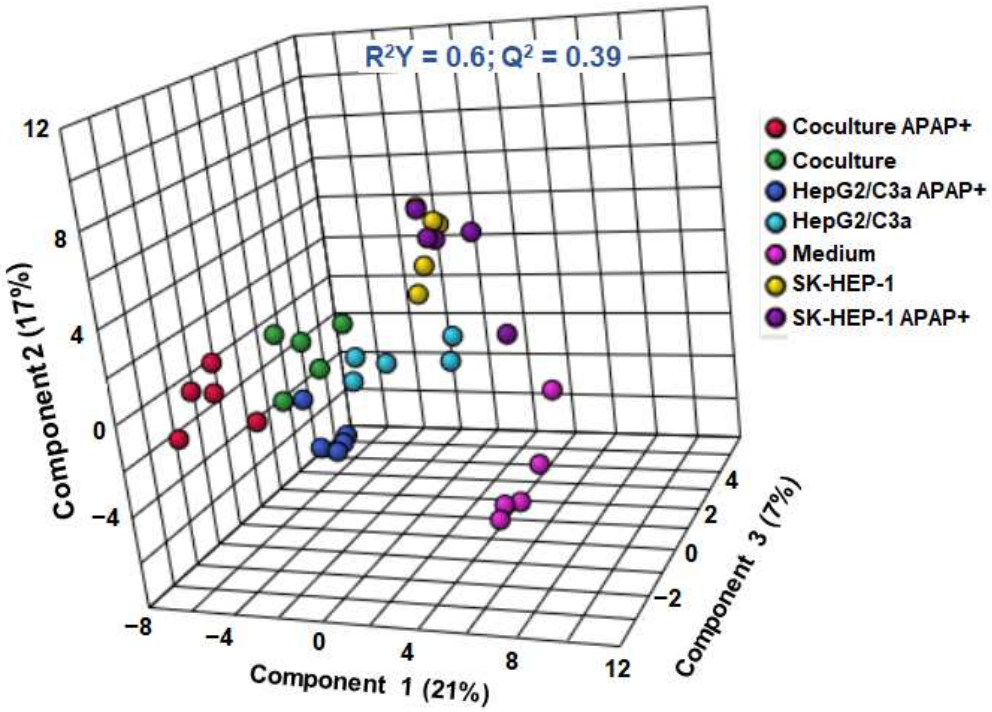

Fig.S5. PLS-DA score plot extracted from the multivariate statistical analysis of metabolomic profiles of all samples. Each dot corresponds to one replicate, n = 5 replicates from three independent experiments.

Table S1. Metabolites identified in the culture media by GC-MS.

Metabolite	PubChem ID	Metabolite	PubChem ID
2,3-butanediol	262	Arabinose	66308
Pyruvic acid	1060	Asparagine	236
Hexanoic acid	8892	Ribose	993
Glycolic acid	757	Xylitol	6912
Alanine	5950	Citrulline	9750
Norvaline	65098	Glycerol 1-phosphate	754
2-hydroxybutyric acid	11266	Deoxyglucose	439268
3-methyl-2-oxobutanoic acid	49	Azelaic acid	2266
Isoleucine	791	Hypoxanthine	790
2-ketoisocaproic acid	70	Citric acid	311
Beta-hydroxyisovalerate	69362	Hippuric acid	464
Valine	6287	Myristic acid	11005
Benzoic acid	243	Methionine sulfoxide	158980
Serine	5951	Fructose	5984
Caprylic acid	379	Tagatose	2724552
Ethanolamine	700	Phenaceturic acid	68144
Glycerol	753	Allantoin	204
Leucine	6106	Pyridoxine	1054
Phosphoric acid	1004	Allose	448388
Threonine	6288	Lysine	5962
Proline	145742	Histidine	6274
Glycine	750	Mannitol	6251
2,3-dihydroxypyridine	28115	Tyrosine	6057
Succinic acid	1110	Sorbitol	5780
Picolonic acid	1018	Galactitol	11850
Glyceric acid	439194	Pantothenic acid	6613
Citraconic acid	638129	Xanthine	1188
Fumaric acid	444972	Palmitoleic acid	445638
Methionine	6137	Palmitic acid	985
Aspartic acid	5960	Uric acid	1175
Beta- alanine	239	Myo-inositol	892
Capric acid	2969	Heptadecanoic acid	10465
Trans-4-hydroxy-L-proline	5810	Tryptophan	6305
Nicotinamide	457	Oleic acid	445639
Malic acid	92824	Stearic acid	5281
Threitol	169019	Cystine	67678
Pyroglutamic acid	7405	Glucose-6-phosphate	439958
Iminodiacetic acid	8897	Arachidic acid	10467
Phenylalanine	994	n-acetylneuraminic acid	445063
Cysteine	594	Sucrose	5988
Creatinine	588	Melibiose	440658
Threonic acid	5460407	Cholesterol	304
Alpha ketoglutaric acid	51	Lactic acid	107689
Ornithine	6262	Oxalic acid	971
Glutamic acid	33032	Urea	1176
Triethanolamine	7618	Glutamine	738
Lauric acid	3893	Glucose	24749

Table S2. Metabolites differentially expressed between the metabolomes of SK-HEP-1 monoculture, HepG2/C3a monoculture, coculture and basal culture medium ($P < 0.05$ and VIP > 1).

Metabolite	P value	Metabolite	P value
Pyridoxine	9.42×10^{-13}	Pyruvic ac	0.0021824
Serine	1.12×10^{-11}	Methionine	0.0021941
2-ketoisocaproic ac	1.80×10^{-11}	Iminodiacetic ac	0.0022303
Glucose	8.08×10^{-11}	Uric ac	0.0022773
Citraconic ac	2.06×10^{-10}	Fructose	0.0023906
Lactic ac	2.35×10^{-10}	Caprylic ac	0.0025456
Allose	5.69×10^{-10}	Glycine	0.0027968
3-methyl-2-oxobutanoic ac	1.93×10^{-9}	Myo-inositol	0.0037971
Hexanoic ac	1.28×10^{-7}	2,3-dihydroxypyridine	0.0041371
Glutamic ac	2.11×10^{-7}	Palmitoleic ac	0.0053894
Succinic ac	5.21×10^{-7}	Deoxyglucose	0.0063703
Glutamine	7.12×10^{-7}	Ethanolamine	0.0077109
Glycerol	8.07×10^{-7}	Threitol	0.0088146
Glucose-6-phosphate	1.02×10^{-6}	Citric ac	0.0089642
Alpha ketoglutaric ac	1.87×10^{-6}	Ornithine	0.0090054
Threonine	2.68×10^{-6}	Galactitol	0.0092401
Alanine	6.83×10^{-6}	Tagatose	0.0093014
Benzoic ac	2.42×10^{-6}	Trans-4-hydroxy-L-proline	0.009467
Ribose	9.62×10^{-5}	Melibiose ou isomaltose	0.010826
2,3-butanediol	9.94×10^{-5}	Asparagine	0.014874
Glycerol 1-phosphate	0.00010663	Beta- alanine	0.020132
Isoleucine	0.00011265	Hypoxanthine	0.025501
Capric ac	0.00011508	Sucrose	0.025737
Arabinose	0.00012185	Xylitol	0.026976
Malic ac	0.00019163	Urea	0.031863
Mannitol	0.00026276	Phenylalanine	0.034987
Oleic ac	0.00064287	Proline	0.041313
Sorbitol	0.00070114	Pantothenic ac	0.046041
Citrulline	0.0019525	Allantoin	0.047924

Table S3. Common and specific metabolites of different cultures exposed to APAP (extracted from Venn's diagram analysis).

Groups	Metabolites
Coculture; HepG2/C3a ; SK-HEP-1	Asparagine, glycerol 1-phosphate, leucine
HepG2/C3a; SK-HEP-1	Glycolic ac, ribose, arabinose
Coculture; HepG2/C3a	Sucrose, mannitol
Coculture; SK-HEP-1	Cysteine, pyroglutamic ac, fumaric ac, ornithine, methionine, oxalic ac
HepG2/C3a	Tyrosine, hypoxanthine, valine, glucose-6-phosphate, cystine
SK-HEP-1	Xanthine, creatinine, uric ac, lauric ac, melibiose, trans-4-hydroxy-L-proline, fructose, pyruvic ac, hexanoic ac, palmitic ac, myristic ac, citrulline, glycerol, galactitol
Coculture	Iminodiacetic ac, threitol, citric ac, threonic ac, succinic ac, glutamic ac, nicotinamide, 3-methyl-2-oxobutanoic ac, deoxyglucose, malic ac, proline, phenylalanine, isoleucine, alpha ketoglutaric ac, 2-ketoisocaproic ac, pyridoxine